EMDNA: An Ensemble Meteorological Dataset for North America

Guoqiang Tang[1], Martyn P. Clark[1,3], Simon Michael Papalexiou[2,4], Andrew J. Newman[5], Andrew W. Wood[5], Dominique Brunet[6], Paul H. Whitfield[1]

[1]Centre for Hydrology, University of Saskatchewan, Canmore, Alberta, Canada

[2]Centre for Hydrology, University of Saskatchewan, Saskatoon, Saskatchewan, Canada

[3]Department of Geography and Planning, University of Saskatchewan, Saskatchewan, Canada

[4]Department of Civil, Geological and Environmental Engineering, University of Saskatchewan, Saskatchewan, Canada

[5]National Center for Atmospheric Research, Boulder, Colorado

[6]Meteorological Research Division, Environment and Climate Change Canada, Toronto, Ontario, Canada

Corresponding author: Guoqiang Tang (guoqiang.tang@usask.ca)

Abstract: Probabilistic methods are useful to estimate the uncertainty in spatial meteorological fields (e.g., the uncertainty in spatial patterns of precipitation and temperature across large domains). In ensemble probabilistic methods, "equally plausible" ensemble members are used to approximate the probability distribution, hence the uncertainty, of a spatially distributed meteorological variable conditioned on the available information. The ensemble members can be used to evaluate the impact of uncertainties in spatial meteorological fields for a myriad of applications. This study develops the Ensemble Meteorological Dataset for North America (EMDNA). EMDNA has 100 ensemble members with daily precipitation amount, mean daily temperature, and daily temperature range at 0.1° spatial resolution (approx. 10-km grids) from 1979 to 2018, derived from a fusion of station observations and reanalysis model outputs. The station data used in EMDNA are from a serially complete dataset for North America (SCDNA) that fills gaps in precipitation and temperature measurements using multiple strategies. Outputs from three reanalysis products are regridded, corrected, and merged using the Bayesian Model Averaging. Optimal Interpolation (OI) is used to merge station- and reanalysis-based estimates. EMDNA estimates are generated using spatiotemporally correlated random fields to sample from the OI estimates. Evaluation results show that (1) the merged reanalysis estimates outperform raw reanalysis estimates, particularly in high latitudes and mountainous regions; (2) the OI estimates are more accurate than the reanalysis and station-based regression estimates, with the most notable improvements for precipitation evident in sparsely gauged regions; and (3) EMDNA estimates exhibit good performance according to the diagrams and metrics used for probabilistic evaluation. We discuss the limitations of the current framework and highlight that further research is needed to improve ensemble meteorological datasets. Overall, EMDNA is expected to be useful for hydrological and meteorological applications in North America. The entire

34   dataset and a teaser dataset (a small subset of EMDNA for easy download and preview) are available at

35   https://doi.org/10.20383/101.0275 (Tang et al., 2020a).

1. Introduction

Precipitation and temperature data are fundamental meteorological variables for a wide variety of geoscientific and applications (Eischeid et al., 2000; Trenberth et al., 2003; Wu et al., 2014; Yin et al., 2018). Accurately estimating spatial meteorological fields is still challenging despite the availability of many measurement/estimation approaches (e.g., meteorological stations, weather radars, and satellite sensors) and the availability of many atmospheric models (Kirstetter et al., 2015; Sun et al., 2018; Hu et al., 2019; Newman et al., 2019a). There is consequently substantial uncertainty in analyses of spatially distributed meteorological variables.

The uncertainty in spatial meteorological estimates depends on both the measurements available and the climate of the region of study. Whilst meteorological stations provide the most reliable observations at the point scale, spatial meteorological estimates based on station data can be uncertain because of both sparse station networks in remote regions and because of measurement errors caused by factors such as evaporation/wetting loss and under-catch of precipitation (Sevruk, 1984; Goodison et al., 1998; Nešpor and Sevruk, 1999; Yang et al., 2005; Scaff et al., 2015; Kochendorfer et al., 2018). Interpolating station data to a regular grid can introduce additional uncertainties, especially in regions where there are strong spatial gradients in meteorological fields. The accuracy of precipitation estimated from ground radars is affected by factors such as beam blockage, signal attenuation, ground clutter, and uncertainties in the representativeness of radar variables to surface rainfall (Dinku et al., 2002; Kirstetter et al., 2015). Moreover, the spatial and temporal coverage of ground radars is limited to large populated areas in most regions of the world. Satellite sensors provide quasi-global estimates of meteorological variables, but their utility can be limited by short sampling periods with insufficient coverage and return frequency, data latency, indirect measurements, imperfect retrieval algorithms, and instrument limitations (Adler et al., 2017; Tang et al., 2016, 2020b). Reanalysis models, which provide long-term global simulations, also contain biases and uncertainties caused by imperfect model representations of physical processes, observational constraints, and the model resolution (Donat et al., 2014; Parker, 2016).

In recent years, numerous deterministic gridded precipitation and temperature datasets based on observed or simulated data from single or multiple sources have become publicly available (Maurer et al., 2002; Huffman et al., 2007; Mahfouf et al., 2007; Daly et al., 2008; Di Luzio et al., 2008; Haylock et al., 2008; Livneh et al., 2013; Weedon et al., 2014; Fick and Hijmans, 2017; Beck et al., 2019; Ma et al., 2020; Harris et al., 2020). Since the uncertainties vary in space and time, deterministic products do not always agree with each other (Donat et al., 2014; Henn et al., 2018; Sun et al., 2018; Newman et al., 2019a; Tang et al., 2020b). The uncertainties can propagate to applications such as hydrological modeling and climate analysis (Clark et al., 2006; Hong et al., 2006; Slater and Clark, 2006; Mears et al., 2011; Rodell et al., 2015; Aalto et al., 2016). Proper understanding of the uncertainties can benefit the objective application of meteorological analyses and further improve existing products, yet few gridded datasets provide such uncertainty estimates (Cornes et al., 2018; Frei and Isotta, 2019).

69   Probabilistic datasets provide alternatives to deterministic datasets for quantitative precipitation and temperature
70   estimation (Kirstetter et al., 2015; Mendoza et al., 2017; Frei and Isotta, 2019). Recently, several ensemble
71   meteorological datasets have become available. For example, Morice et al. (2012) develop the observation-based
72   HadCRUT4 global temperature datasets with 100 members. Caillouet et al. (2019) develop the Spatially COherent
73   Probabilistic Extended Climate dataset (SCOPE Climate) with 25 members in France. Newman et al. (2015, 2019b,
74   2020) continually extend the probabilistic estimation methodology proposed by Clark and Slater (2006), and produce
75   ensemble precipitation and temperature datasets in the contiguous USA (CONUS), the Hawaii Islands, and Alaska
76   and Yukon, respectively. Moreover, several widely used deterministic datasets now have ensemble versions in view
77   of the advantages of probabilistic estimates. Cornes et al. (2018) developed the ensemble version (100 members) of
78   the Haylock et al. (2008) Europe-wide E-OBS temperature and precipitation datasets. Khedhaouiria et al. (2020)
79   developed the experimental High-Resolution Ensemble Precipitation Analysis (HREPA) for Canada and the northern
80   part of the CONUS with 24 members, which can be regarded as an experimental ensemble version of the Canadian
81   Precipitation Analysis (CaPA; Mahfouf et al., 2007; Fortin et al., 2015).

82   Our objective is to develop an Ensemble Meteorological Dataset for North America (EMDNA) from 1979 to 2018.
83   To improve the quality of estimates in sparsely gauged regions, station data and reanalysis outputs are merged to
84   generate gridded precipitation and temperature estimates. Then, ensemble estimates are produced using the
85   probabilistic method described by Clark and Slater (2006) and Newman et al. (2015, 2019b, 2020). EMDNA has 100
86   members and contains daily precipitation amount, mean daily temperature (Tmean), and daily temperature range
87   (Trange) at 0.1° spatial resolution. Minimum and maximum temperature can be calculated from Tmean and Trange.
88   It is expected that the EMDNA will be useful for a variety of applications in North America.

2. Datasets

90   Station observations are often subject to temporal discontinuities caused by missing values and short record lengths
91   (Kemp et al., 1983). This study uses station precipitation and minimum/maximum temperature data from the Serially
92   Complete Dataset for North America (SCDNA; Tang et al., 2020c), which is open-access on Zenodo
93   (https://doi.org/10.5281/zenodo.3735533; Access Date: July 25, 2020). Serially complete datasets improve the quality
94   of spatial interpolation estimates compared to raw station observations with data gaps (Longman et al., 2020; Tang et
95   al., 2021). Tmean and Trange are calculated from minimum and maximum temperature data. In SCDNA, raw
96   measurements undergo strict quality control checks, and data gaps are filled by combining estimates from multiple
97   strategies (including quantile mapping, spatial interpolation, machine learning, and multi-strategy merging). SCDNA
98   uses reanalysis estimates as the auxiliary data to ensure temporal completeness in sparsely gauged regions. The
99   production of SCDNA has nine steps: (1) matching reanalysis estimates and station data, (2) selecting qualified
100   neighboring stations, (3) building empirical cumulative density functions (CDFs), (4) estimation based on 16 strategies
101   for each day of the year, (5) independent validation, (6) merging estimates from the 16 strategies, (7), climatological
102   bias correction, (8) evaluation of SCDNA, and (9) final quality control (Tang et al., 2020c). SCDNA covers the period
103   from 1979 to 2018 and has 24,615 precipitation stations and 19,579 temperature stations. We select precipitation and

104   temperature because they are used in many hydrometeorological studies and are measured by a large number of

105   meteorological stations, while other variables (e.g., humidity and wind speed) are only measured by a much smaller

106   collection of stations.

107   Station-based gridded meteorological estimates usually rely on a certain number of neighboring stations surrounding

108   the target grid cell. For most regions in CONUS, the search radius to find 20 or 30 neighboring stations (lower and

109   upper limits for station-based gridded estimates in Sect. 3.1) is smaller than 100 km (Fig. 1). For the regions north of

110   to 50°N or south of 20°N, however, the search radius required to find 20 or 30 neighboring stations is much larger,

111   and even exceeds 1,000 km in the Arctic Archipelago. The sparse station network at higher latitudes motivates our

112   decision to optimally combine station data with reanalysis products.

113   The reanalysis products used in this study include the fifth generation of European Centre for Medium-Range Weather

114   Forecasts (ECMWF) atmospheric reanalyses of the global climate (ERA5; Hersbach et al., 2020), the Modern-Era

115   Retrospective analysis for Research and Applications, Version 2 (MERRA-2; Gelaro et al., 2017), and the Japanese

116   55-year Reanalysis (JRA-55; Kobayashi et al., 2015). The three widely used products are chosen because of their high

117   spatiotemporal resolutions and suitable time length. The spatial resolutions of ERA5, MERRA-2, and JRA-55 are

118   0.25°×0.25°, 0.5°×0.625°, and ~55 km, respectively. Their start years are 1979, 1980, and 1958, respectively.

119   Therefore, only ERA5 and JRA-55 are used for 1979 throughout this study. Although reanalysis models assimilate

120   observations from various sources, they differ from station measurements in many aspects (Parker, 2016) and often

121   contain large uncertainties as shown by assessment and multi-source merging studies (e.g., Donat et al., 2014; Lader

122   et al., 2016; Beck et al., 2017, 2019; Tang et al., 2020b). The dependence of reanalysis estimates on station data may

123   have a negative effect on the merging of reanalysis products (Section 3.2) because the reanalysis dataset which

124   assimilates more station data could be given higher weight. The potential dependence, however, is not considered in

125   this study because of the limited understanding of the dependence between reanalysis estimates and station

126   observations. Moreover, none of the reanalysis datasets assimilate precipitation data from stations.

127   The elevation data are sourced from the 3 arc-second resolution Multi-Error-Removed Improved-Terrain digital

128   elevation model (MERIT DEM; Yamazaki et al., 2017).

129
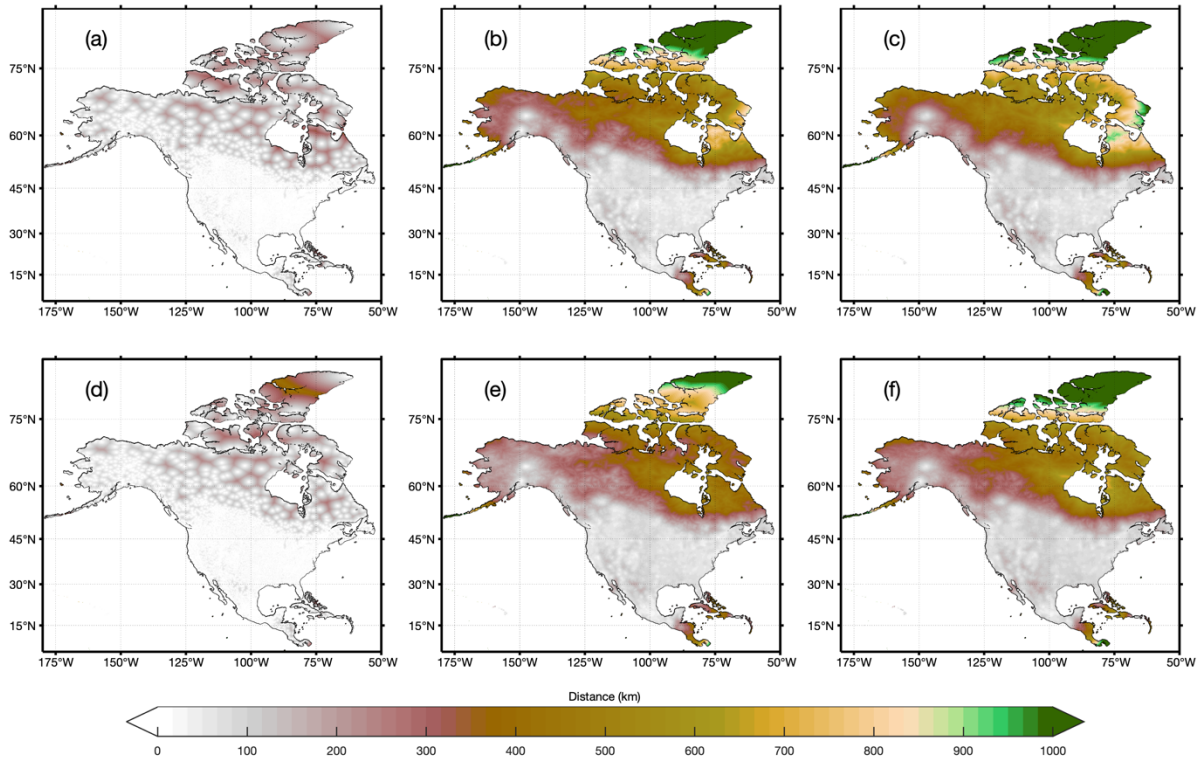
Figure 1. The color of each 0.1° grid indicates the radius to find (a) one, (b) 20, and (c) 30 neighboring stations for precipitation (a-c) and temperature (d-f).

3. Methodology

The estimate of a variable at a specific location and time step can be regarded as a random value following a probability distribution. The probability density functions (PDFs) of variables such as Tmean and Trange can be approximated using the normal distribution. Their value x for a target location and time step is expressed as:

$$x \sim N(\mu, \sigma^2) \tag{1}$$

where μ is the mean value and σ is the standard deviation. Probabilistic estimates of Tmean or Trange can be realized by sampling from this distribution. In a spatial meteorological dataset, the distribution parameters vary with space and time, and the spatial variability is related to the nature of variables and gridding (interpolation) methods. The performance of gridding methods is critical because accurate estimation of μ can reduce systematic bias and smaller σ means narrower spread.

Precipitation is different from Tmean and Trange because it can be intermittent from local to synoptic scales and its distribution is both highly skewed and bounded at zero. Following Papalexiou (2018) and Newman et al. (2019b), the CDF of precipitation can be expressed as below:

144

$$F_X(x) = (1 - p_0)F_{X|X>0}(x) + p_0, \quad for \ x \geq 0 \tag{2}$$

145   where $F_X(x)$ is the CDF for $x \geq 0$, $F_{X|X>0}(x)$ is the CDF for $x > 0$, and p_0 is the probability of zero precipitation.

146   The probability of precipitation (PoP) is $1 - p_0$. The CDF $F_{X|X>0}(x)$ is often approximated using the normal

147   distribution after applying suitable transformation functions to observed precipitation. Clark and Slater (2006) perform

148   the normal quantile transformation using an empirical CDF from station observations. Newman et al. (2015) apply a

149   power-law transformation. Newman et al. (2019b) adopts the Box-Cox transformation, that is,

$$x' = \frac{x^\lambda - 1}{\lambda} \tag{3}$$

150   where λ is set to 1/3 following Newman et al. (2019b) and Fortin et al. (2015). Eq. (1) applies to x', enabling the

151   probabilistic estimation of precipitation. Unlike Newman et al. (2019b) that uses transformed precipitation throughout

152   the production, this study only uses Box-Cox transformation when the assumption of normality is necessary (Sect.

153   3.2.4 and 3.3) to reduce the error introduced by the back transformation. The limitations and alternative choices of

154   precipitation transformation are discussed in Sect. 5.2.

155   In summary, seven space- and time-varying parameters (μ and σ for three variables and PoP) should be obtained to

156   realize probabilistic estimation. Our method to develop probabilistic meteorological estimates is summarized in Fig.

157   2a. We apply four main steps to produce EMDNA: (1) station-based regression estimates (Sect. 3.1), (2) the regridding,

158   downscaling, bias correction and merging of three reanalysis products (Sect. 3.2), (3) optimal interpolation-based

159   merging of reanalysis and station-based regression outputs, and the bias correction of the resulting precipitation

160   estimates (Sect. 3.3), and (4) the production of probabilistic estimates in the form of spatial meteorological ensembles

161   (Sect. 3.4).

162
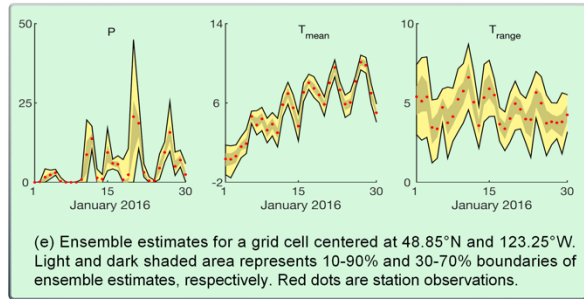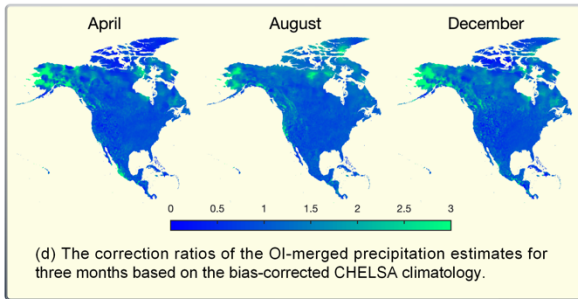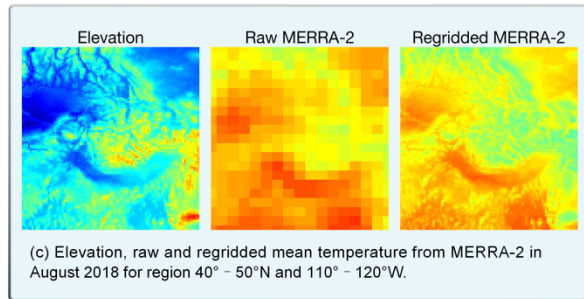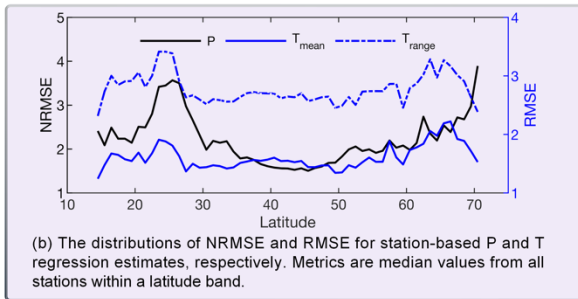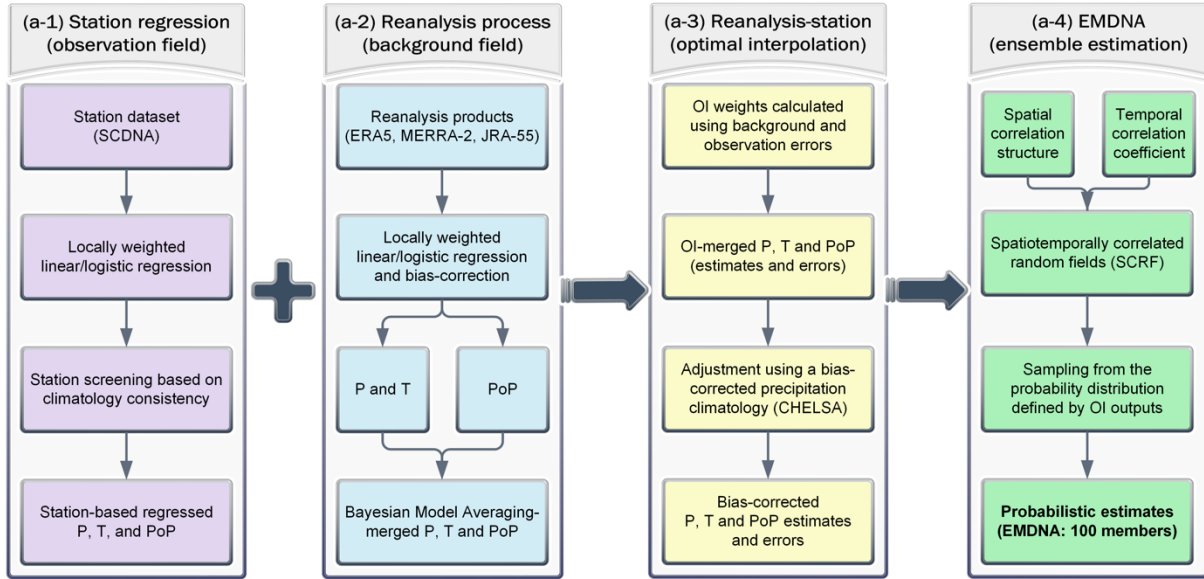
Figure 2. (a) The flowchart outlining the main steps for producing EMDNA. P represents precipitation and T represents temperature. (b-e) demonstrate output examples from (a-1 to -4), respectively. (b) Latitudinal distribution of the root mean square error (RMSE) for temperature and normalized RMSE (NRMSE) for precipitation (Sect. 3.1). (c) Example showing the mean temperature of MERRA-2 before and after regridding (Sect. 3.2). (d) The correction ratios calculated using precipitation climatology from the bias-corrected CHELSA (Sect. 3.3). (e) Example of the ensemble-based distributions of precipitation and temperature estimates from EMDNA (Sect. 3.4).

3.1 Regression estimates from station data

Clark and Slater (2006) and Newman et al. (2015, 2019b) use locally weighted linear regression and logistic regression to obtain gridded temperature and gridded precipitation estimates which are used as parameters in Eq. (1). However, for high-latitude regions in North America where stations are scarce (Fig.1), such gridded estimates based only on station data could contain large uncertainties (Fig. 2b) due to the long distances needed to assemble a sufficient sample of stations to form the regressions. This study uses optimal interpolation (OI) to merge data from stations and reanalysis models. In this section, we only obtain regression estimates and their errors at the locations of stations, which are used as inputs to OI in Sect. 3.3.

3.1.1 Locally weighted linear regression

Daily precipitation amount, Tmean, and Trange are estimated for all stations based on the locally weighted linear regression (also known as the geographically weighted regression). Let x_o be the station observation for variable X (precipitation, Tmean, and Trange), the regression estimate $\hat{x}$ for the target point and time step is obtained as below:

$$x_o = \hat{x} + \varepsilon = \beta_0 + \sum_{i=1}^{n} A_i \beta_i + \varepsilon \tag{4}$$

where A_i is the ith time-invariant topographic attribute (or predictor variables), β_0 and β_i are regression coefficients estimated using ordinary least squares, and ε is the residual (or error term). The topographic attributes are latitude, longitude, and elevation for Tmean and Trange. For precipitation, two more topographic attributes (west-east and south-north slopes) are used to account for windward and leeward slope precipitation differences. An isotropic Gaussian low-pass filter is used to smooth DEM before calculating slopes, which can reduce the influence of noise in a high-resolution DEM on the large-scale topographic effect of precipitation (Newman et al., 2015). Ideally, the scale of this smoothing reflects the scale at which terrain most directly influences precipitation or temperature spatial patterns; in this case the filter bandwidth is 180 km.

For a target station point, $\hat{x}$ is obtained based on data from neighboring stations. Newman et al. (2015, 2019b) used 30 neighboring stations, without controlling for maximum station distance. The very low station density in high-latitude regions makes this configuration infeasible, hence this study adopts a relatively flexible criterion for selecting neighboring stations: (1) finding at most 30 stations within a fixed search radius (400 km), and (2) if fewer than 20 stations are found, extending the search radius until 20 stations are found. The lower threshold is set to 20 to ensure that linear/logistic regression is robust. To incorporate local dependence, a tricube weighting function is used to calculate the weight $w_{i,j}$ between the target station i and the neighboring station j.

$$w_{i,j} = [1 - (\frac{d_{i,j}}{d_{max}})^3]^3 \tag{5}$$

where $d_{i,j}$ is the distance between i and j, and d_{max} depends on the maximum distance ($d_{i,j}^{max}$) between i and all its neighboring stations. If $d_{i,j}^{max}$ is smaller than 100 km, d_{max} is set to 100 km; otherwise, d_{max} is set to $d_{i,j}^{max} + 1$ km

198   (Newman et al., 2015, 2019b). The cubic weight function is smoother compared to functions such as exponential
199   functions and inverse distance functions, indicating that $w_{i,j}$ degrades with distance in a relatively slow way which
200   generally leads to smooth spatial variations of variables. The comparison of different weight functions could be a
201   direction for future research. Regression coefficients are estimated by weighted least squares method (described in
202   Appendix A).

203   We found that a small number of observation stations show a climatology that is notably statistically different from
204   surrounding stations, which could cause an adverse effect on gridded estimates, particularly in sparsely gauged regions.
205   Strategies to identify and exclude such stations are summarized in Appendix B.

3.1.2   Locally weighted logistic regression

207   PoP is estimated using the locally weighted logistic regression by fitting binary precipitation occurrence to topographic
208   attributes:

$$\text{PoP} = \frac{1}{1 + \exp(-\beta_0 + \sum_{i=1}^{n} A_i \beta_i)} \tag{6}$$

209   The topographic attributes (A_i) are the same as those used by precipitation regression. Appendix A describes the
210   method to estimate regression coefficients.

211   The errors of precipitation, temperature, and PoP estimates for all stations are calculated as the difference between
212   regression estimates and station observations using the leave-one-out cross-validation procedure (also known as the
213   jackknife procedure). The leave-one-out evaluation could be affected by the distributions of stations in some cases.
214   For example, two stations with very close distance may both show very high accuracy in the leave-one-out evaluation
215   (this is a problem for all station-based evaluation methods).

3.2 Regridding, correction, and merging of reanalysis datasets

217   The three reanalysis datasets (ERA5, MERRA-2, and JRA-55) have different spatial resolutions and contain
218   systematic biases. In this section, we discuss steps taken to (1) re-grid all reanalysis datasets to the resolution of
219   EMDNA (0.1°); (2) perform a correction to remove the systematic bias in original estimates; and (3) merge the three
220   reanalysis datasets to produce a background field that improves over any individual reanalysis dataset, in support of
221   the reanalysis-station merging described in Sect. 3.3.

3.2.1   Regridding of reanalysis datasets

223   Precipitation, Tmean, and Trange are regridded to 0.1° using locally weighted regression (Fig. 2c). Latitude, longitude,
224   and elevation are used as predictor variables for simplicity. Precipitation or temperature lapse rates are implicitly
225   considered by involving elevation in the regression. Raw reanalysis data from a 5×5 space window (i.e., 25 coarse-
226   resolution grids) centered by the 0.1° target grid are used to perform the regression. Each grid is represented using its

227   center point. This regridding method has been proven effective in previous studies (Xu et al., 2015; Duan and Li, 2016;
228   Lu et al., 2020). Reanalysis estimates are also regressed to the locations of all stations to facilitate evaluation and
229   weight estimation in the following steps, which can avoid the scale mismatch caused by using point-scale observations
230   to evaluate 0.1° gridded estimates (Tang et al., 2018a).

231   We also tested other regridding methods such as the nearest neighbor, bilinear interpolation, and temperature lapse
232   rate-based downscaling (Tang et al., 2018b). Results (not shown) indicated that their performance is generally inferior
233   to the locally weighted regression with respect to several accuracy metrics.

3.2.2   Probability of precipitation estimation

235   Reanalysis precipitation can exhibit large biases in the number of wet days because the models often generate many
236   light precipitation events. To overcome this limitation, we designed two methods for determining the occurrence of
237   reanalysis precipitation. The first is to use positive thresholds to determine precipitation occurrence. The threshold
238   was estimated in two ways, namely by forcing reanalysis precipitation (1) to have the same number of wet days with
239   station data, or (2) to achieve the highest critical success index (CSI). Gridded thresholds can be obtained through
240   interpolation and used to discriminate between precipitation events or non-events. However, this method can only
241   obtain binary occurrence instead of continuous PoP between zero and one. The second method is based on univariate
242   logistic regression. The amount of reanalysis precipitation is used as the predictor and the binary occurrence from
243   station data is used as the predictand. The logistic regression is implemented for each reanalysis product in the same
244   way as Sect. 3.1.2. The comparison between the threshold-based method and the logistic regression-based method
245   shows the latter achieves higher accuracy. Therefore, we adopt the univariate logistic regression to estimate PoP for
246   each reanalysis product in this study. The possible bias caused by station measurements is not considered.

3.2.3   Bias correction of reanalysis datasets

248   Considering reanalysis products contain systematic biases (Clark and Hay, 2004; Mooney et al., 2011; Beck et al.,
249   2017; Tang et al., 2018b, 2020b), the linear scaling method (also known as multiplicative/additive correction factor;
250   Teutschbein and Seibert, 2012) is used to correct reanalysis precipitation, Tmean, and Trange estimates. Reanalysis
251   PoP is not corrected because station information has been incorporated in the logistic regression. Let x_r be the
252   reanalysis estimate for variable X, the corrected estimate for a target grid/point i is calculated as:

$$x_{r,i}^* = \begin{cases} x_{r,i} + \dfrac{\sum_{j=1}^{m} w_{i,j}(\bar{x}_{o,j} - \bar{x}_{r,j})}{\sum_{j=1}^{m} w_{i,j}} & \text{additive correction} \\[4ex] x_{r,i} \dfrac{\sum_{j=1}^{m} w_{i,j}\dfrac{\bar{x}_{o,j}}{\bar{x}_{r,j}}}{\sum_{j=1}^{m} w_{i,j}} & \text{multiplicative correction} \end{cases} \quad (7)$$

253   where $x_{r,i}^*$ is the corrected reanalysis estimate, $w_{i,j}$ is the distance-based weight (Eq. (5)), and $\bar{x}_{o,j}$ and $\bar{x}_{r,j}$ are the
254   climatological mean for each month (e.g., all January from 1979 to 2018) from station observations and reanalysis

255   estimates for the jth neighboring station, respectively. The additive correction is used for Tmean and Trange, and the

256   multiplicative correction is used for precipitation. The number of neighboring stations (m) is set to 10, which is smaller

257   than that used for linear or logistic regression (Sect. 3.1) but should be enough for bias correction. The upper bound

258   of $\frac{\bar{x}_{o,j}}{\bar{x}_{r,j}}$ is set to 10 to avoid over-correction in some cases (Hempel et al., 2013).

259   Linear scaling can be performed at monthly (Arias-Hidalgo et al., 2013; Herrnegger et al., 2018; Willkofer et al., 2018)

260   or daily (Vila et al., 2009; Habib et al., 2014) time scales by replacing $\bar{x}_{o,j}$ and $\bar{x}_{r,j}$ by the monthly mean (e.g., January

261   in one year) or daily values. We compared the performance of corrections at different scales and found that monthly-

262   or daily-scale corrections acquire more accurate estimates than the climatological correction. The climatological

263   correction was adopted because (1) it preserves the absolute/relative trends better than daily or monthly corrections,

264   and (2) the OI merging (Sect. 3.3) adjusts daily variability of estimates, which compensates for the limitation of

265   climatological correction and makes daily/monthly-scale correction unnecessary.

266   Quantile mapping is another widely used correction method (Wood et al., 2004; Cannon et al., 2015). We compared

267   quantile mapping and linear scaling and found that they are similar in statistical accuracy, while quantile mapping

268   achieves better probability distributions with much smaller Hellinger distance (Hellinger, 1909) which is a metric used

269   to quantify the similarity between estimated and observed probability distributions. Nevertheless, quantile mapping

270   could result in spatial smoothing of precipitation and temperature, particularly in high-latitude regions where stations

271   are few. For example, Ellesmere Island, the northernmost island of the Canadian Arctic Archipelago, usually shows

272   lower temperature in inland regions. However, quantile mapping will erase this gradient because reanalysis grids for

273   this island are corrected based on stations on the coast. To ensure the authenticity of spatial distributions, quantile

274   mapping is not used in this study.

3.2.4   Merging of reanalysis datasets

276   The three reanalysis products are merged using the Bayesian Model Averaging (BMA, Hoeting et al., 1999), which

277   has proved to be effective in fusing multi-source datasets (Chen et al., 2015; Ma et al., 2018a, b). According to the

278   law of total probability, the PDF of the BMA estimate can be written as:

$$p(E) = \sum_{r=1}^{3} p(E|x_r^*, x_o) \cdot p(x_r^*|x_o) \tag{8}$$

279   where E is the ensemble estimate, x_r^* (r=1, 2, 3) is the bias-corrected estimate from three reanalysis products,

280    $p(E|x_r^*, x_o)$ is the predicted PDF based only on a specific reanalysis product, and $p(x_r^*|x_o)$ is the posterior probability

281   of reanalysis products given the station observation x_o. The posterior probability $p(x_r^*|x_o)$ can be identified as the

282   fractional BMA weight w_r with $\sum_{r=1}^{3} w_r = 1$. BMA prediction can be written as the weighted sum of individual

283   reanalysis products.

284   For Tmean and Trange, $p(E|x_r^*, x_o)$ can be regarded as the normal distribution $g(E|\theta_r)$ defined by the parameter

285      $\theta_r = \{\mu_r, \sigma_r^2\}$, where μ_r is the mean and σ_r^2 is the variance (Duan and Phillips, 2010). For precipitation, if we apply

286   Box-Cox transformation (Eq. (3)) to positive events (>0) and exclude zero events, its distribution is approximately

287   normal, and $p(E|x_r^*, x_o)$ can be represented using $g(E|\theta_r)$. Therefore, Eq. (8) can be written as:

$$p(E) = \sum_{r=1}^{3} w_r \cdot g(E|\theta_r) \qquad (9)$$

288   There are different approaches to infer w_r and θ_r (Schepen and Wang, 2015). This study uses the log-likelihood

289   function to estimate the parameters (Duan and Phillips, 2010; Chen et al., 2015; Ma et al., 2018b). The Expectation-

290   Maximization algorithm (Raftery et al., 2005) can be applied to estimate parameters by maximizing the likelihood

291   function. BMA weights are obtained for all stations and each month. Gridded weights are obtained using the inverse

292   distance weighting interpolation.

293   Merging multiple datasets could affect the probability distributions and extreme characteristics of original datasets.

294   This is not a major concern because the merged reanalysis data are further adjusted by station data in OI merging (Sect.

295   3.3), a later step in the EMDNA process. Also, the probabilistic estimation of ensemble members (Sect. 3.4) has a

296   large effect on estimates of extreme events.

297   Gridded errors of BMA-merged estimates are necessary to enable optimal interpolation (Sect. 3.3). The error

298   estimation is realized using a two-layer cross-validation (Appendix C).

299   **3.3 Optimal Interpolation-based merging of reanalysis and station data**

300   **3.3.1   Optimal Interpolation**

301   OI has proven to be effective in merging multiple datasets (Sinclair and Pegram, 2005; Xie and Xiong, 2011) and has

302   been applied in operational products such as CaPA (Mahfouf et al., 2007; Fortin et al., 2015) and the China Merged

303   Precipitation Analysis (CMPA, Shen et al., 2014, 2018). Let x_A be the OI analysis estimate. The OI analysis estimate

304      $(x_{A,i})$ for a target grid/point i and time step is obtained by adding an increment to the first guess of the background

305      $(x_{B,i})$. The increment is a weighted sum of the difference between observation and background values at neighboring

306   stations.

$$x_{A,i} = x_{B,i} + \sum_{j=1}^{m} w_j(x_{O,j} - x_{B,j}) \qquad (10)$$

307   where $x_{O,j}$, $x_{B,j}$, and w_j are the observed value (subscript O), background value (subscript B), and weight for the jth

308   neighboring station. Let x_T be the true value, the errors of observed and background values are $\varepsilon_{O,j} = x_{O,j} - x_{T,j}$ and

309      $\varepsilon_{B,j} = x_{B,j} - x_{T,j}$ (or $\varepsilon_{B,i} = x_{B,i} - x_{T,i}$), respectively. Assuming that (1) the observation and background errors are

310   unbiased with an expectation of zero and (2) there is no correlation between background and observation errors, the

311   weights that minimize the variance of the analysis errors can be obtained by solving:

$$\mathbf{w}(\mathbf{R} + \mathbf{B}) = \mathbf{b} \qquad\qquad (11)$$

312   where $\mathbf{w}$ is the vector of w_j ($j = 1,2, ..., \text{m}$), $\mathbf{R}$ and $\mathbf{B}$ are $m \times m$ covariance matrices of $\varepsilon_{O,j}$ and $\varepsilon_{B,j}$, respectively,

313   and $\mathbf{b}$ is the $m \times 1$ vector of covariance between $\varepsilon_{B,i}$ and $\varepsilon_{B,j}$. The background provided by reanalysis models

314   assimilates observations in the production and is corrected in a way using station data (described in Sect. 3.2.3), which

315   may affect the soundness of the second assumption. The effect of this slight violation, however, is rather small

316   according to our results and previous studies (Xie and Xiong, 2011; Shen et al., 2014b, 2018).

317   Different approaches can be used to implement OI. For example, Fortin et al. (2015) used raw station observations as

318   x_O, and assumed that the background error is a function of error variance and correlation length, and the observation

319   error is a function of error variance. The variances and correlation length are obtained by fitting a theoretical variogram

320   using station observations. Xie and Xiong (2011) and Shen et al. (2014) use station-based gridded estimates as x_O,

321   and assume that the background error variance is a function of precipitation intensity, the cross-correlation of

322   background errors is a function of distance, and the observation error variance is a function of precipitation intensity

323   and gauge density. The parameters of those functions are estimated based on station data in densely gauged regions.

324   In this study, we adopt a novel design that calculates weights based on error estimation, a feature that is enabled by

325   the probabilistic nature of the observational dataset. Regression estimates and their errors at station points (Sect. 3.1)

326   are used as x_O and ε_O, respectively. BMA-merged reanalysis estimates and their errors (Sect. 3.2) are used as x_B and

327   ε_B, respectively. We do not use gridded regression estimates because (1) $x_{O,j} - x_{B,j}$ will show weak variation if

328   neighboring stations are replaced by neighboring grids, and (2) estimates of weights $\mathbf{w}$ could be unrealistic because

329   of the spatial smoothing of interpolated regression errors. The advantages of this design are (1) weights and inputs

330   closely match each other and (2) weights in sparsely gauged regions are not determined by parameters fitted in densely

331   gauged regions. In regions with few stations, the errors of regression estimates could be larger than reanalysis estimates,

332   resulting in a smaller contribution from regression estimates and a larger contribution from reanalysis estimates, which

333   is the complementary effect we expect by involving reanalysis datasets in EMDNA.

334   The Box-Cox transformation is applied to precipitation estimates. Then, precipitation, PoP, Tmean, and Trange

335   estimates provided by OI are used as μ and PoP required for generating meteorological ensembles.

336   ### 3.3.2   Error of OI-merged estimates

337   Variance is a necessary parameter to enable ensemble estimation. The variance σ^2 is represented using the mean

338   squared error of OI estimates in this study. First, the error of OI analysis estimates ($\varepsilon_A = x_A - x_o$) is obtained for all

339   stations using the leave-one-out strategy. Then, the σ_i^2 for the ith grid is obtained as a weighted sum of squared errors

340   from neighboring stations:

$$\sigma_i^2 = \frac{\sum_{j=1}^{m} w_{i,j} (\varepsilon_{A,j})^2}{\sum_{j=1}^{m} w_{i,j}} \qquad (12)$$

341   where $\varepsilon_{A,j}$ is the difference between the station observation and OI estimate at the jth neighboring station, and $w_{i,j}$ is

342   the weight (Eq. (5)).

343   ### 3.3.3   Correction of precipitation under-catch

344   Considering station precipitation data usually contain measurement errors such as wind-induced under-catch

345   particularly in high-latitude and mountainous regions, OI-merged precipitation is further adjusted using the

346   Precipitation Bias Correction (PBCOR) dataset produced by Beck et al. (2020). The PBCOR climatology infers the

347   long-term precipitation (without rain-snow separation) using a Budyko curve and streamflow observations collected

348   from seven national and international sources, among which the Global Runoff Data Centre (GRDC), the U.S.

349   Geological Survey (USGS), and the Water Survey of Canada Hydrometric Data (HYDAT) are data sources in North

350   America. The streamflow stations are scarce in high latitude regions and absent in Greenland. Three corrected datasets

351   are provided, including WorldClim, version 2 (WorldClim V2; Fick and Hijmans, 2017), the Climate Hazards Group

352   Precipitation Climatology, version 1 (CHPclim V1; Funk et al., 2015) and Climatologies at High Resolution for the

353   Earth's Land Surface Areas, version 1.2 (CHELSA V1.2; Karger et al., 2017). The water balance-based method of

354   Beck et al. (2020) considers all measurement errors (e.g., under-catch and wetting/evaporation loss) as a whole and

355   under-catch is the major error source in many regions. Note that the rain gauge catch error includes both under-catch

356   and over-catch. The potential over-catch could be caused by splash of rain or blow snow collected on the wind shield

357   (Folland, 1988; Zhang et al., 2019). Since over-catch is less common compared to under-catch and the PBCOR dataset

358   does not consider over-catch, the bias correction in this study only addresses the under-catch problem. Moreover, the

359   water balance estimates of precipitation under-catch do not consider non-contributing areas of river basins (e.g.,

360   endorheic sub-catchments), which are common in the Canadian Prairies and the northern Great Plains in the USA.

361   Although the three datasets show similar precipitation distributions after bias correction, CHELSA V1.2 is used

362   because its period (1979–2013) is most similar to our study period (1979–2018). The correction of OI-merged

363   precipitation is performed in two steps: (1) the ratio between bias-corrected CHELSA V1.2 and OI-merged long-term

364   monthly precipitation is calculated at the 0.1° resolution during 1979–2013, and (2) daily OI-merged precipitation

365   estimates during 1979–2018 are scaled using the corresponding monthly ratio map. The bias correction notably

366   increases precipitation in northern Canada and Alaska (Fig. 2d) where precipitation under-catch is often significant

367   due to the large proportion of snowfall. The uncertainties of gridded estimates are typically larger in high-latitude

368   sparsely gauged regions and topographically elevated regions, which is partly related to the increased proportion of

369   snowfall and hence larger gauge catch errors.

3.4 Ensemble generation

3.4.1 Spatiotemporally correlated random fields

Spatially correlated random fields (SCRFs) are used to sample from the probability distributions of precipitation and temperature. The SCRFs are produced using the following three steps. First, the spatial correlation structure is generated based on an exponential correlation function:

$$c_{i,j} = \exp\left(-\frac{d_{i,j}}{C_{len}}\right) \tag{13}$$

where $d_{i,j}$ is the distance between grids i and j, and C_{len} is the spatial correlation length determined for each climatological month based on regression using station data for precipitation, Tmean, and Trange, separately. The spatial correlation structure is generated using the conditional distribution approach. Every point is conditioned on previously generated points which are determined using a nested simulation strategy to improve the calculation efficiency (Clark and Slater, 2006).

Second, the spatially correlated random field ($\mathbf{R}_t$) for the tth time step is generated by sampling from the normal distribution with the mean value and standard deviation depending on the random numbers of previously generated grids (Clark and Slater, 2006).

Third, the SCRF is generated by incorporating spatial and temporal correlation relationships. Let ρ_{TM} and ρ_{TR} be the lag-1 auto-correlation for Tmean and Trange, respectively, ρ_{CR} be the cross-correlation between Trange and precipitation, $\mathbf{R}_{t-1,TM}$, $\mathbf{R}_{t-1,TR}$ and $\mathbf{R}_{t-1,PR}$ be the SCRF for the $(t-1)$th time step for Tmean, Trange, and precipitation, respectively, the SCRF for tth time step following (Newman et al., 2015) is written as:

$$\begin{cases} \mathbf{R}_{t,TM} = \rho_{TM}\mathbf{R}_{t-1,TM} + \sqrt{1-\rho_{TM}^2}\,\mathbf{R}_{t-1,TM} \\ \mathbf{R}_{t,TR} = \rho_{TR}\mathbf{R}_{t-1,TR} + \sqrt{1-\rho_{TR}^2}\,\mathbf{R}_{t-1,TR} \\ \mathbf{R}_{t,PR} = \rho_{CR}\mathbf{R}_{t,TR} + \sqrt{1-\rho_{CR}^2}\,\mathbf{R}_{t-1,PR} \end{cases} \tag{14}$$

3.4.2 Probabilistic estimation

Probabilistic estimates are produced using the probability distribution $N(\mu, \sigma^2)$ in Eq. (1) and $\mathbf{R}$ in Eq. (14). For Tmean and Trange, the SCRF ($\mathbf{R}_{TM}$ and $\mathbf{R}_{TR}$) is directly used as the standard normal deviate (R_X). The estimate (x_e) for the ensemble member e is written as:

$$x_e = \mu + R_X \cdot \sigma \tag{15}$$

391   For precipitation, an additional step is to judge whether an event occurs or not according to OI-merged PoP and the

392   estimated probability from the SCRF. Let $F_N(x)$ be the CDF of the standard normal distribution, $F_N(\mathrm{R}_{PR})$ is the

393   cumulative probability corresponding to the random number R_{PR}. If $F_N(\mathrm{R}_{PR})$ is larger than p_0, the scaled cumulative

394   probability of precipitation (p_{cs}) is calculated as:

$$p_{cs} = \frac{F_N(\mathrm{R}_{PR}) - p_0}{1 - p_0} \tag{16}$$

395   The probabilistic estimate for precipitation can be expressed as:

$$x_e = \begin{cases} 0 & if & F_N(\mathrm{R}_{PR}) \le p_0 \\ \mu + F_N^{-1}(p_{cs}) \cdot \sigma & if & F_N(\mathrm{R}_{PR}) > p_0 \end{cases} \tag{17}$$

396   **3.5 Evaluation of probabilistic estimates**

397   Independent stations that are not used in SCDNA are used to evaluate EMDNA because the leave-one-out strategy is

398   too time-consuming to evaluate probabilistic estimates. GHCN-D stations with precipitation or temperature records

399   less than eight years are extracted because SCDNA restricts attention to stations with at least eight-year records. In

400   total, 15,018 precipitation stations and 2,455 temperature stations are available for independent testing.

401   The Brier skill score (BSS; Brier, 1950) is used to evaluate probabilistic precipitation estimates. The continuous ranked

402   probability skill score (CRPSS) is used to evaluate probabilistic temperature estimates. Their definitions are described

403   in Appendix D.

404   Furthermore, the reliability and discrimination diagrams are used to assess the behavior of probabilistic precipitation

405   estimates. The reliability diagram shows the conditional probability of an observed event (precipitation above a

406   threshold) given the probability of probabilistic precipitation estimates. In a reliability diagram, a perfect match has

407   all points located on the 1-1 line. The discrimination diagram shows the PDF of probabilistic precipitation estimates

408   for different observed categories. For precipitation, two categories are defined: events or non-events, i.e., observed

409   precipitation above or below a threshold. The difference between PDF curves of events or non-events represents the

410   degree of discrimination. Larger discrimination is preferred. The PDF for non-event/event should be maximized at the

411   probability of zero/one.

412   **4. Results**

413   **4.1 Comparison between raw and merged reanalysis estimates**

414   The three raw reanalysis estimates are regridded, corrected for bias, and merged. In this section, we directly compare

415   raw and BMA-merged estimates. The evaluation is performed for all stations using the two-layer cross-validation

416   strategy. The correlation coefficient (CC), root mean square error (RMSE), and normalized RMSE (NRMSE) are used

417   as evaluation metrics. RMSE is sued for Tmean, and NRMSE is used for precipitation and Trange to remove patterns

418   caused by climatology.

419   For precipitation, the three reanalysis products show the highest CC in CONUS and the lowest CC in Mexico (Fig. 3).

420   The slight spatial discontinuity of CC along the Canada-USA border and the USA-Mexico border (Fig. 3 and 6) is

421   caused by the inconsistent reporting time of stations. Daily precipitation from reanalysis products is accumulated from

422   0 to 24 UTC, while stations from different countries or regions usually have different UTC accumulation periods

423   (Beck et al., 2019; Tang et al., 2020a). NRMSE is higher in central CONUS and Mexico compared to other regions.

424   Overall, ERA5 outperforms MERRA-2 followed by JRA-55.

425   BMA-merged precipitation estimates show higher accuracy than all reanalysis products (Fig. 3). The improvement of

426   CC and NRMSE is the most evident in the Rocky Mountains, while for MERRA-2, the improvement is also obvious

427   in central CONUS. ERA5 is the closest to BMA estimates concerning CC and NRMSE. The improvement of BMA

428   estimates against ERA5 is more prominent in the high-latitude regions. Specifically, the mean CC increases by 0.05

429   and 0.07 in regions southern and northern to 55°N, respectively. The corresponding decrease of mean NRMSE is 0.15

430   and 0.21, respectively.

431
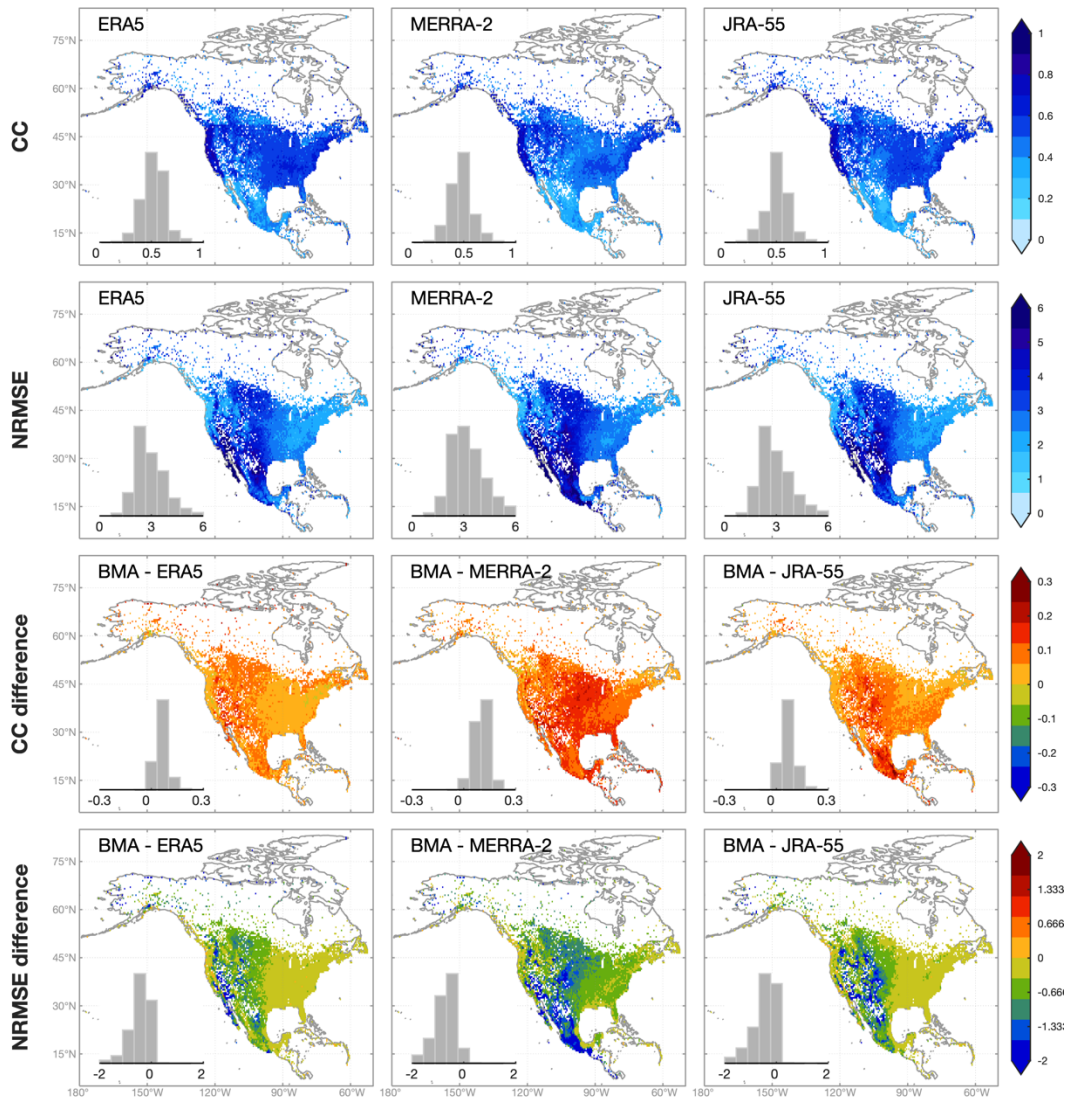
Figure 3. The spatial distributions and histograms of CC (the first row) and NRMSE (the second row) based on raw reanalysis precipitation estimates (ERA5, MERRA-2, and JRA-55). The improvement of BMA-merged estimates against raw reanalysis estimates is shown in the third and fourth rows. The maps are at the 0.5° resolution, and the value of each 0.5° grid point is the median metric of all stations located within the grid.

The CC of reanalysis Tmean estimates is close to one in most regions of North America (Fig. 4) and still above 0.9 in Mexico where the CC is the lowest. According to RMSE, Tmean estimates have the largest error in western North America because coarse-resolution raw reanalysis estimates cannot reproduce the variability of temperature caused by elevation variations. The rank of three reanalysis products for Tmean is the same as that for precipitation with ERA5 being the best one. BMA estimates show higher CC than reanalysis products particularly in Mexico, while the improvement of RMSE is the most notable in the Rocky Mountains. For a few stations, the RMSE of BMA estimates

442 is slightly worse than raw reanalysis estimates (Fig. 4) because the downscaling of reanalysis temperature could
443 occasionally magnify the error in low-altitude regions (Tang et al., 2018b).

444 For Trange, BMA estimates show much larger improvement than Tmean, while the differences of CC and NRMSE
445 are relatively evenly distributed (Fig. 5). The improvement of BMA estimates against JRA-55 estimates is especially
446 large. In general, BMA is effective in improving the accuracy of reanalysis precipitation and temperature estimates.
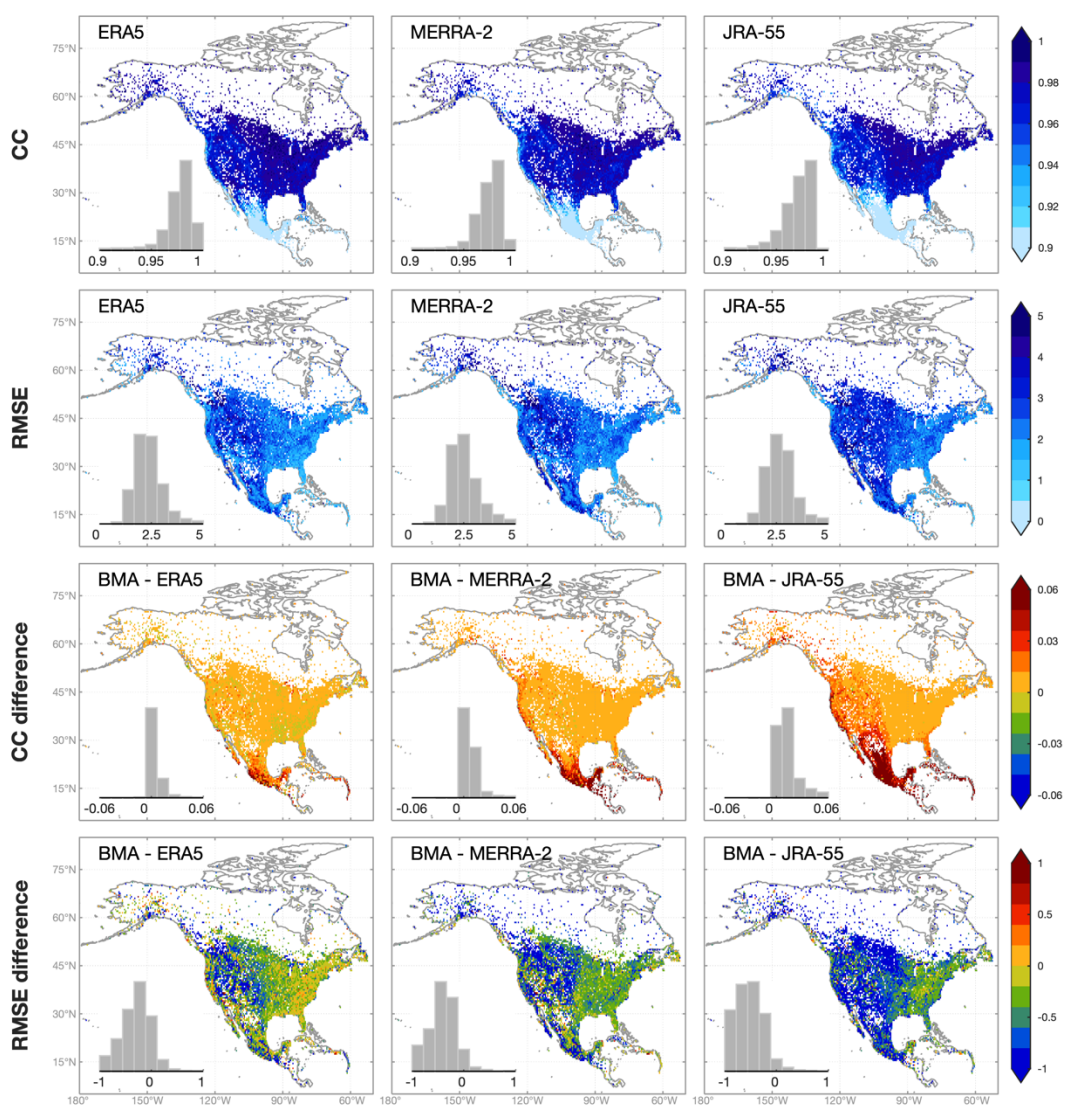
447

448 Figure 4. Same with Figure 3, but for mean temperature.

449
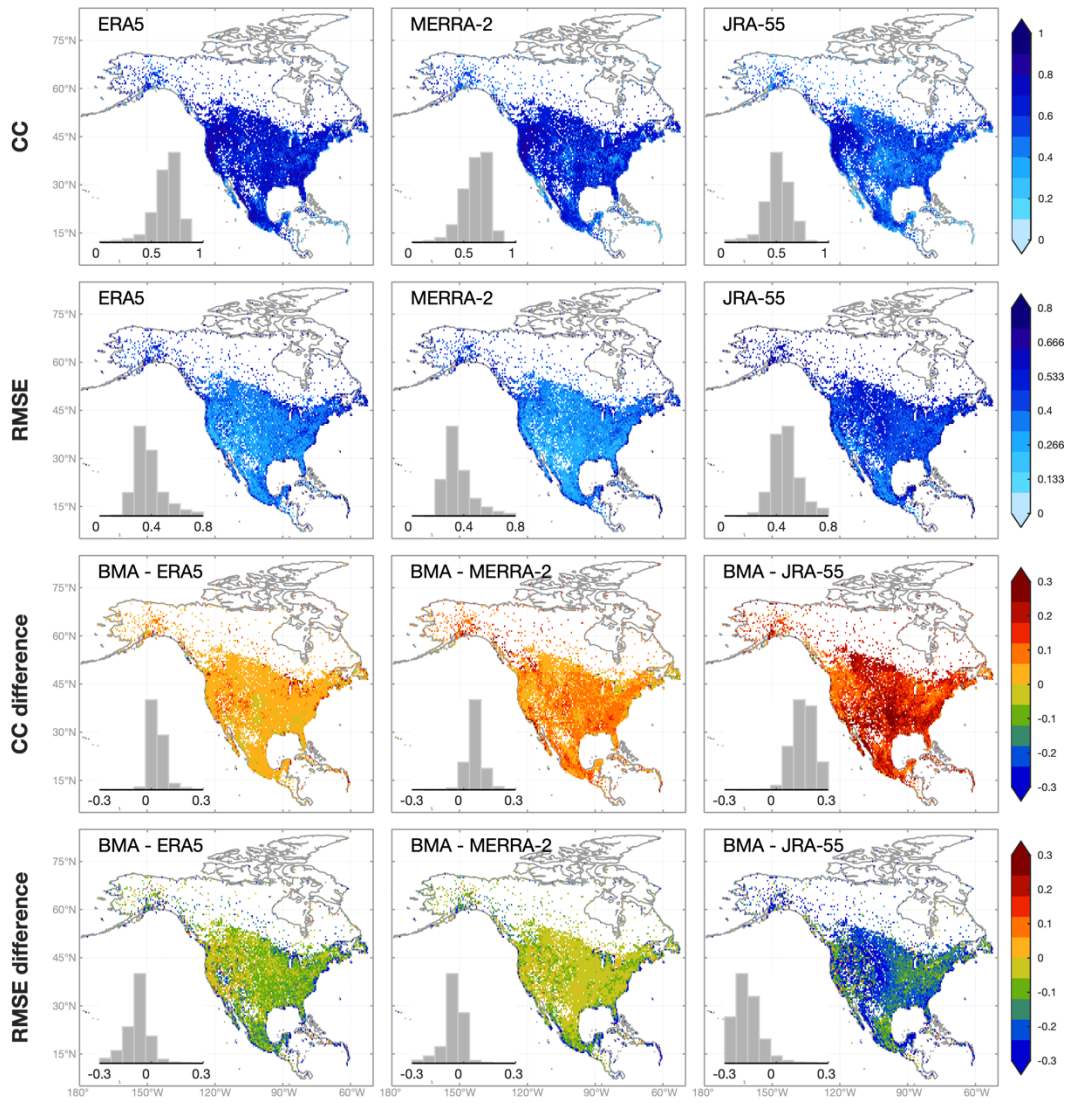
Figure 5. Same with Figure 3, but for daily temperature range.

4.2 The performance of optimal interpolation

Optimal interpolation is used to combine station-based estimates with reanalysis estimates. The performance of OI-merged precipitation and temperature estimates is compared to the background (BMA-merged reanalysis estimates; Fig. 6) and observation (station-based regression estimates; Fig. 7) inputs. To better show the spatial variations of the improvement of OI estimates, RMSE for precipitation and Trange is normalized using the mean value (termed as NRMSE), while Tmean is evaluated using RMSE.

Overall, OI estimates are more accurate than merged reanalysis or station regression estimates for all variables across North America. Comparing OI estimates to reanalysis estimates, for precipitation, Tmean, and Trange, the mean CC is improved by 0.24, 0.02, and 0.15, respectively, and the mean RMSE is reduced by 1.88 mm/d, 0.52℃, and 0.87℃,

460   respectively. The improvement of OI estimates against station estimates is smaller with the mean CC increasing by

461   0.06, 0.01 and 0.05, and the mean RMSE decreasing by 0.56 mm/d, 0.18℃, and 0.29℃ for precipitation, Tmean, and

462   Trange, respectively.

463   OI can utilize the complementarity between station and reanalysis estimates. For example, according to CC, the

464   improvement of OI estimates against reanalysis estimates is larger in the eastern than the western CONUS, while the

465   improvement against station estimates is larger in western than eastern CONUS. This means that although station

466   estimates generally show higher accuracy than reanalysis estimates, station estimates face more severe quality

467   degradation in mountainous regions. Moreover, the latitudinal curves of CC and NRMSE in Fig. 6 and 7 indicate that

468   the improvement of OI estimates against reanalysis estimates decreases as the latitude increases from southern

469   CONUS to northern Canada, while the improvement against station estimates shows a reverse trend.

470   For Tmean, the CC improvement for OI estimates is the largest in Mexico and decreases from low to high latitudes,

471   while based on RMSE, the improvement increases with latitude. For Trange, the latitudinal variation exhibits a similar

472   pattern with precipitation for regions north of 50°N, with larger/smaller improvement in higher latitudes against

473   station/reanalysis estimates. For regions south of 50°N, the improvement of CC and NRMSE against station estimates

474   shows different trends.

475   Station-based estimates often have lower accuracy in regions with scarce stations (i.e., high-latitude North America),

476   while reanalysis estimates could have less dependence on station densities due to the compensation of physically-

477   based models. Therefore, OI merging is particularly useful in sparsely gauged regions.
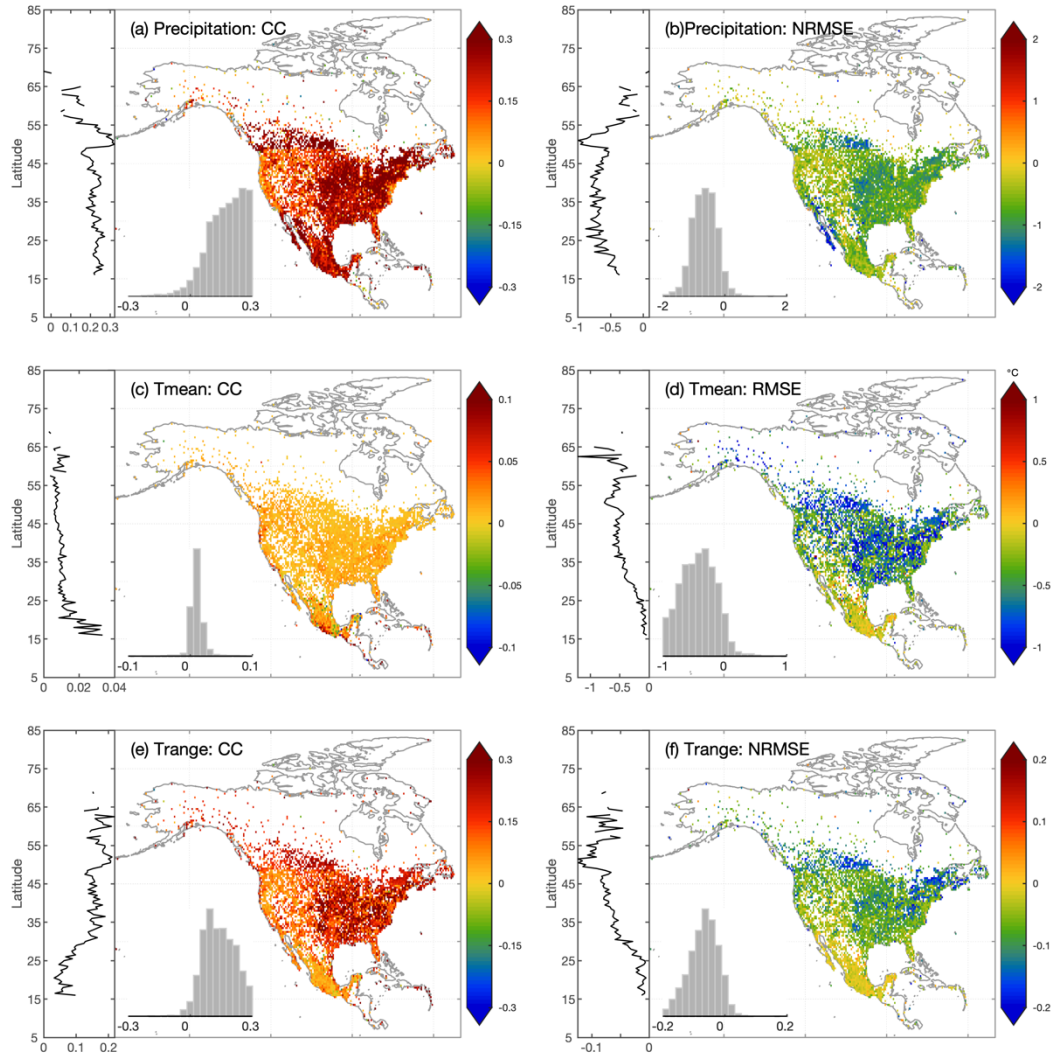
478

479 Figure 6. The differences of (a) CC and (b) NRMSE (normalized RMSE) between OI-merged precipitation estimates

480 and BMA-merged reanalysis precipitation estimates. The latitudinal distributions of metrics are attached on the left

481 side, showing the median value for 0.5° latitude bands. (c-d) are the same with (a-b) but for mean temperature and

482 RMSE is not normalized. (e-f) are the same with (a-b) but for daily temperature range.

483
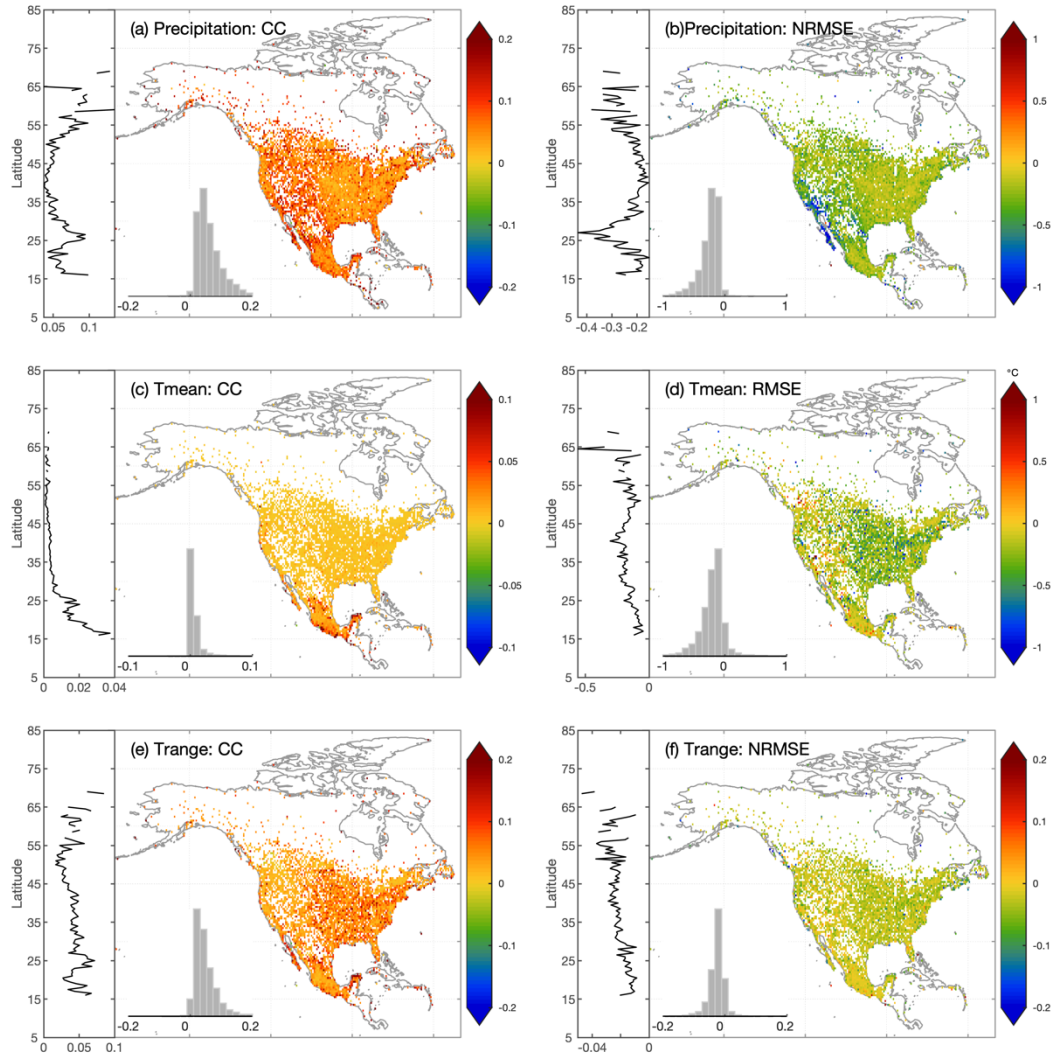
Figure 7. Similar with Figure 6, but the differences are between OI-merged precipitation estimates and station-based regression precipitation estimates.

4.3 Evaluation of probabilistic estimates

The distributions of the OI and ensemble precipitation, Tmean, and Trange estimates in June 2016 are shown in Fig. 8. Compared with OI precipitation estimates, ensemble precipitation estimates show generally consistent but less smooth distributions because of the relatively short spatial correlation length in the warm season. For Tmean and Trange, OI and ensemble estimates show very similar spatial distributions. Precipitation shows the largest standard deviation, while Tmean shows the smallest, because the standard deviation is determined by the errors of OI estimates.

The PoP from station observations and ensemble estimates is compared based on stations with at least 5-year-long records from 1979 to 2018 (Fig. 9). The comparison cannot represent climatological PoP (Newman et al., 2019b) due to short time length of independent stations (Sect. 3.5). Overall, EMDNA estimates show similar PoP distributions with station observations. The PoP in Canada is slightly overestimated because (1) the quality of EMDNA is lower in

regions with fewer stations and (2) point-scale station observations could underestimate the PoP at a larger scale (e.g., 0.1° grids) as shown by Tang et al. (2018a).
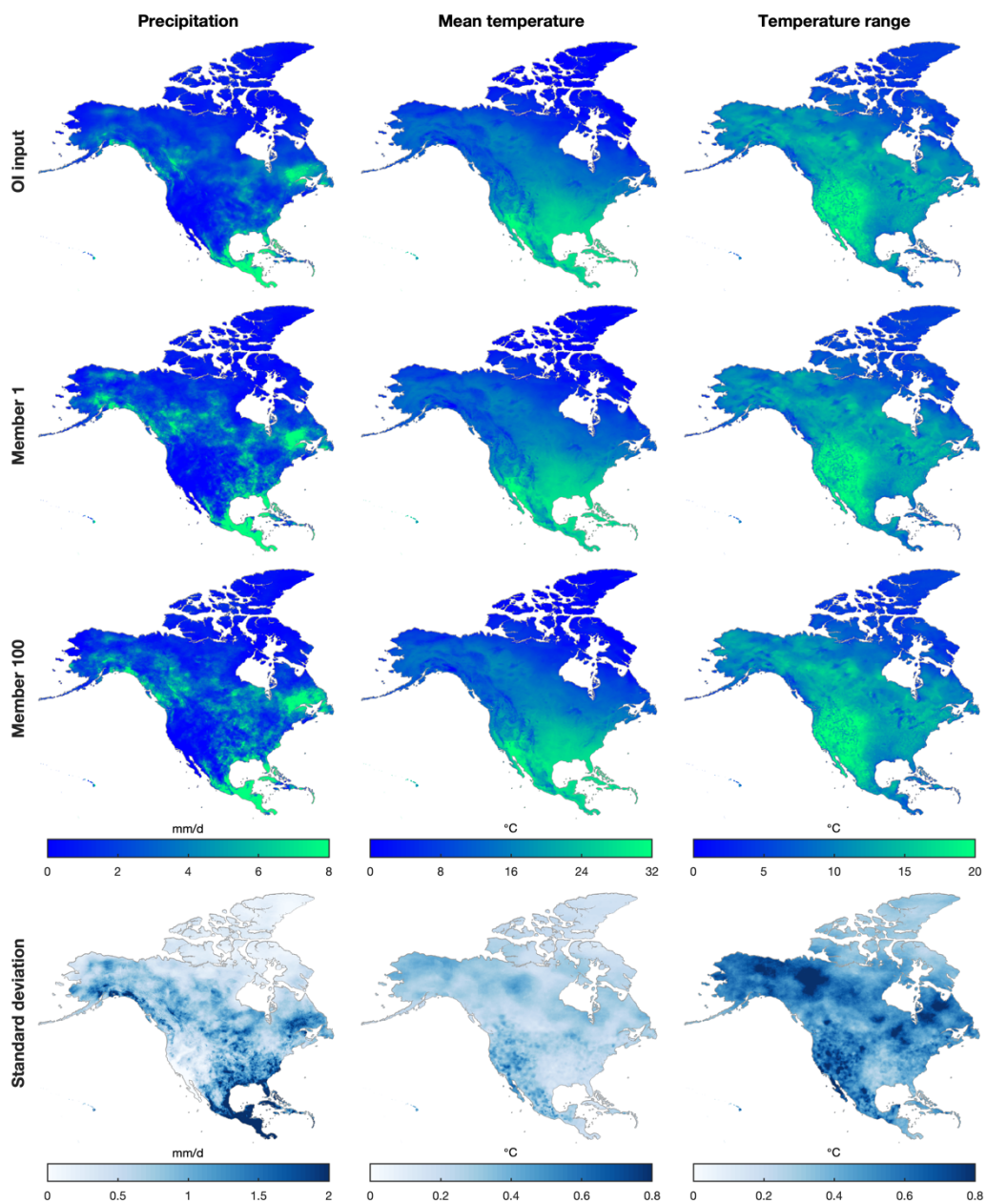
Figure 8. The distributions of average values from precipitation (the first column), mean daily temperature (the second column), and daily temperature range (the third column) averaged over the period 1-30 June 2016. The first to third rows represent estimates from OI-merged inputs, ensemble member 1, and ensemble member 100. The fourth row represents the standard deviation of all the 100 members for one month (June 2016).

503
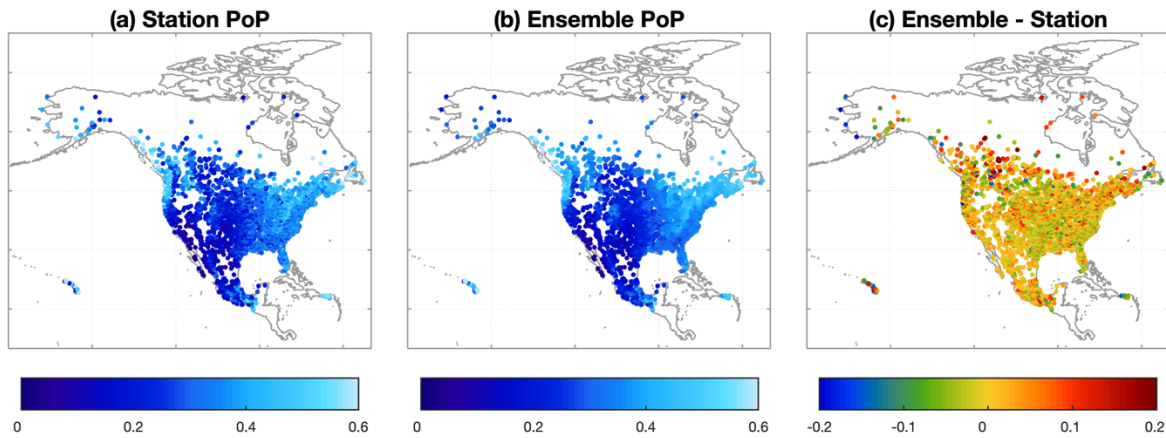
Figure 9. The probability of precipitation (PoP) from (a) station observations and (b) concurrent EMDNA ensemble estimates with their differences shown in (c). Stations with at least 5-year-long records from 1979 to 2018 are involved in the comparison.

The discrimination diagram (Fig. 10) shows that ensemble precipitation assigns the highest occurrence frequency at the lowest estimated probability for non-precipitation events, and the performance becomes better as the threshold increases from 0 to 50 mm. For precipitation events, ensemble estimates show the highest frequency at the highest estimated probability for the thresholds of 0, 10, and 25 mm, while as the threshold increases, the frequency curve becomes skewed to the lower estimated probability. This problem is also seen in Clark and Slater (2006) and Newman et al. (2015). Ensemble precipitation shows good reliability for all precipitation thresholds with the points located at or close to the 1-1 line (Fig. 10). At low and high estimated probabilities of occurrence, ensemble precipitation shows slight wet bias. The reliability performance does not show clear dependence with thresholds.

515
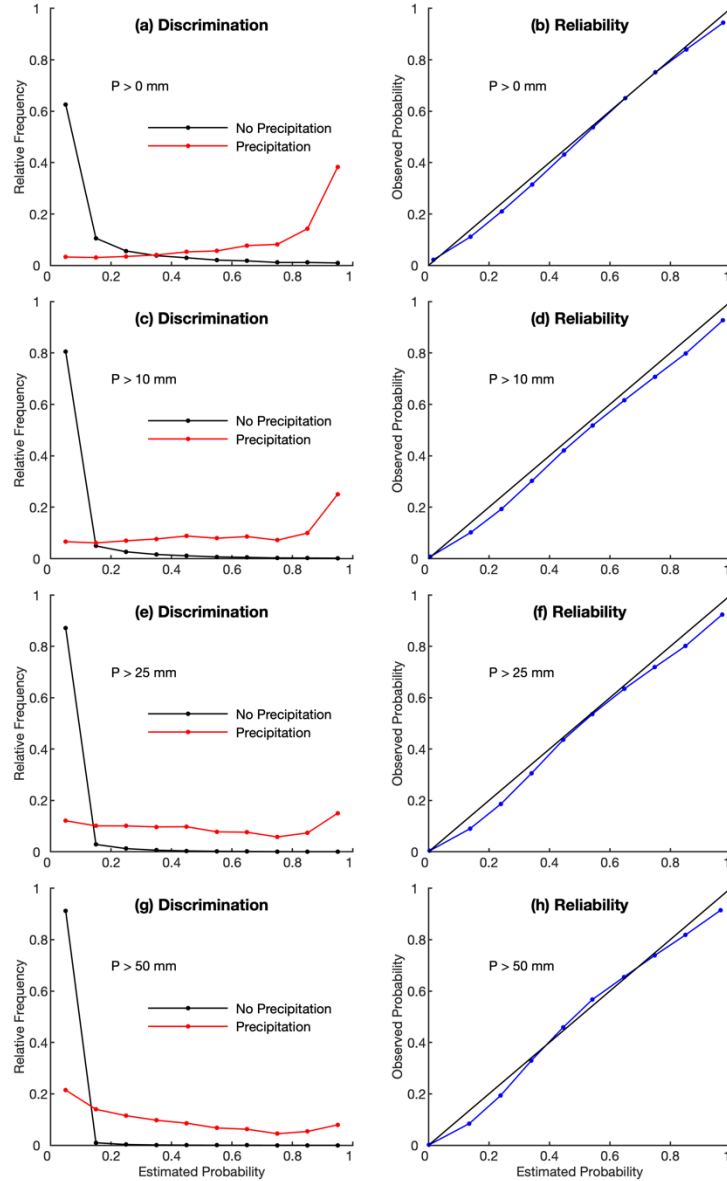
Figure 10. The discrimination and reliability diagrams based on ensemble precipitation estimates. Four rain/no rain thresholds (0, 10, 25, 50 mm) are used.

The BSS for precipitation and CRPSS for Tmean and Trange are shown in Fig. 11. In most cases, ensemble precipitation shows the highest frequency when BSS is above 0.5. As the precipitation threshold increases, the BSS values decrease. The median BSS values are 0.62, 0.54, and 0.46 for the thresholds of 0, 10, and 20 mm/d, respectively. We note that a small number of cases show BSS values smaller than zero, indicating that the ensemble estimated probability is worse than climatological probability. A low BSS value usually occurs in regions where precipitation is hard to estimate (e.g., Rocky Mountains) resulting in inaccurate parameters of Eq. (1).

524 The BSS for all thresholds shows a clear increasing trend from 1979 to 2018 (Fig. 11b) because the observed
525 precipitation samples from SCDNA increase during this period (Fig. 2 in Tang et al. (2020c)). The increasing trend
526 of BSS is particularly prominent from 2003 to 2009, during which precipitation samples in the USA experience the
527 greatest increase (Tang et al., 2020c). The results show that although infilled station data contribute to higher station
528 densities, observation samples still have a significant effect on gridded data estimation.

529 Tmean shows high CRPSS for most cases with the frequency peak occurring at ~0.8. The CRPSS of Trange is much
530 lower with the peak occurring at ~0.6. The median CRPSS for Tmean and Trange is 0.74 and 0.51, respectively.
531 Trange shows lower CRPSS probably because the bias direction (i.e., overestimation or underestimation) of daily
532 minimum and maximum temperature could be different, resulting in the larger bias of Trange than Tmean. Analyses
533 show that among stations with negative CRPSS, most are located in Mexico due to the degraded quality of temperature
534 estimates (Sect. 4.1 and 4.2). The long-term variation of CRPSS is not shown because independent temperature
535 stations are insufficient to support validation between 1986 and 2010.

536
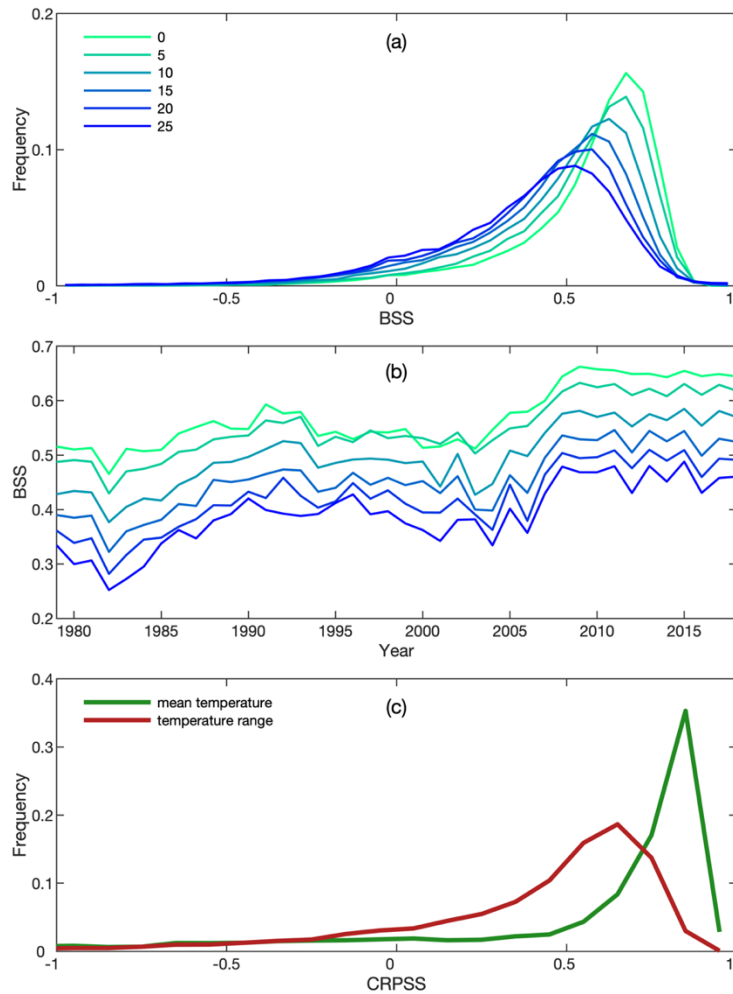
Figure 11. (a) The frequency distributions of the Brier Skill Score (BSS) for precipitation corresponding to rain/no rain thresholds from 0 to 25 mm/d. (b) The distributions of BSS for precipitation from 1979 to 2018. For each year, the median value of all stations is used. (c) The frequency distributions of the continuous ranked probability skill score (CRPSS) for daily mean temperature and daily temperature range.

5. Discussion

This study presents the framework for producing an ensemble precipitation and temperature dataset over North America. Although we have tested multiple choices of methods (Sect. 3) and overall the product shows good performance (Sect. 4), the methodology still has limitations that need to be improved through continued efforts.

5.1 Implementation of OI

OI is used to merge reanalysis outputs and station data. To implement OI-based merging, a critical step is to estimate the weights. Previous studies usually adopt empirical error or variogram functions and fit the parameters using station observations (e.g., CaPA (Fortin et al., 2015) and CMPA (Shen et al., 2018)); then the parameters are constant for the whole study area in the actual application.

In this study, we proposed a novel design, which uses station-based regression estimates as the observation field and calculates weights by directly solving the weight functions based on observation and background errors. Compared with methods that use station data as the observation field, our method is characterized by inferior estimation of the observation field but realistic estimation of weights. The close linkage between the observation field and the weights could benefit OI estimates but comparing different OI implementations is still meaningful and necessary considering that OI has been widely used and is the core algorithm of some operational products.

Furthermore, regression estimates show worse performance in regions with fewer stations. More advanced interpolation methods that can utilize climatology information and comprehensively consider topographic and atmospheric conditions (Daly et al., 2008; Newman et al., 2019b; Newman and Clark, 2020) should be examined in future studies.

5.2 Probabilistic estimation

Power transformations (e.g., Box-Cox and root/cubic square) with fixed parameters have proven to be useful in precipitation estimation and dataset production (Fortin et al., 2015, 2018; Cornes et al., 2018; Khedhaouiria et al., 2020; Newman et al., 2020). The Box-Cox transformation with a constant parameter is applied following Fortin et al. (2015) and Newman et al. (2019b, 2020). A fixed parameter, however, cannot ensure that transformed precipitation is normally distributed everywhere as is desirable.

We tested a series of additional parametric and non-parametric transformations based on power functions, logarithmic functions, or a mix of both, and optimized the parametric transformation functions (including Box-Cox) for every grid

568   by minimizing the objective function which is the sum of squared L-skewness and L-kurtosis (Papalexiou and

569   Koutsoyiannis, 2013). Theoretically, compared to a Box-Cox transformation with a fixed parameter, the optimized

570   functions can obtain precipitation series closer to the normal distribution which should benefit probabilistic estimation,

571   while the evaluation results show that the Box-Cox transformation with a fixed parameter is better at probabilistic

572   estimation than optimized functions. We suggest there are three reasons for this: (1) the standard deviation in Eq. (1)

573   is obtained by interpolating OI errors (Sect. 3.2.2) from neighboring stations, whereas the optimized transformation

574   parameters could be different at those stations, (2) zero precipitation is excluded during optimization to avoid invalid

575   transformation or optimization, which reduces the number of stations for every time step and thus degrades the quality

576   of the spatial interpolation, and (3) the errors caused by back transformation could be large if the optimized

577   transformation is too powerful. More efforts are needed to resolve this problem.

578   There are other potential directions for improvement. For example, SCRF is generated from Gaussian distributions,

579   while other choices such as copulas functions (Papalexiou and Serinaldi, 2020) show potential in probabilistic

580   estimation. The spatial correlation length is constant for the whole study area following Newman et al. (2015, 2019b),

581   which may introduce uncertainties for a large domain. Overall, studies related to the production of ensemble

582   meteorological datasets are still insufficient, particularly for large areas. More studies are needed to clarify the critical

583   issues in large-scale probabilistic estimation and explore the effect of parameter/method choices on probabilistic

584   estimates.

585   5.3   Alternate data sources

586   The quality of source data (station observations and reanalysis models) primarily determines the quality of output

587   datasets. The density of stations has a critical effect on the accuracy of the observation field and probabilistic estimates.

588   While SCDNA collects data from multiple datasets, efforts are ongoing to expand the database by involving station

589   sources such as provincial station networks in Canada.

590   For reanalysis products, ERA5, MERRA-2, and JRA-55 are regridded using locally weighted linear regression to meet

591   the target resolution. There are some choices for future improvement, such as (1) adopting/developing better

592   downscaling methods or (2) utilizing outputs from high-resolution re-analysis products or forecasting models such as

593   ERA5-Land (Muñoz-Sabater et al., 2021) or the Arctic System Reanalysis (Bromwich et al., 2018). Moreover,

594   including other data sources such as satellite and weather radar estimates is also an opportunity for regions with

595   adequate sample coverage.

596   5.4   Precipitation under-catch

597   Although station precipitation observations are used as the reference in this study, these values are subject to

598   measurement errors such as wetting loss, wind-induced under-catch, and trace precipitation. Station temperature

599   measurements also contain errors due to microclimate and sensor design, which is generally small and not discussed

600   here. The under-catch of precipitation is particularly severe in high latitudes and mountains due to the stronger wind

601   and frequent snowfall (Sevruk, 1984; Goodison et al., 1998; Nešpor and Sevruk, 1999; Yang et al., 2005; Scaff et al.,

602 2015; Kochendorfer et al., 2018). For example, underestimation of precipitation could be larger than 100% in Alaska
603 (Yang et al., 1998). Bias correction of station precipitation data should consider many factors such as gauge types,
604 precipitation phase, and environmental conditions, which would be very complicated when a large number of sparsely
605 distributed stations are involved over the whole of North America.

606 The under-catch correction used in this study relies on bias-corrected precipitation climatology produced by Beck et
607 al. (2020), which infers the long-term precipitation using a Budyko curve and streamflow observations. The bias-
608 corrected precipitation climatology, however, is less accurate in northern Canada where streamflow stations are few
609 (Beck et al., 2020). The streamflow data used by the bias-corrected climatology also contain uncertainties (Hamilton
610 and Moore, 2012; Kiang et al., 2018) related to factors such as streamflow derivation methods (e.g., rate curves) and
611 measurement instruments. In addition, this correction method aims to constrain the total precipitation amount and
612 cannot distinguish between rainfall and snowfall which show different gauge catch performance. Data users can realize
613 rain-snow classification using approaches such as temperature threshold-based methods and reanalysis model-based
614 snowfall proportion. Moreover, as mentioned earlier, the water balance estimates of precipitation under-catch do not
615 consider non-contributing areas of river basins. Whilst various under-catch correction methods (e.g., Fuchs et al., 2001;
616 Beck et al., 2020; Newman et al., 2020) exist, further studies are needed to compare these solutions considering their
617 effectiveness and availability of input data in a large domain.

6. Data availability

619 The EMDNA dataset is available at https://doi.org/10.20383/101.0275 (Tang et al., 2020a) in netCDF format.
620 Individual ensemble member, ensemble mean, and ensemble spread of precipitation, Tmean, and Trange are provided.
621 Since the 100 members are equally plausible, users can download fewer members if the storage space and processing
622 time are limited. The deterministic OI estimates of precipitation, PoP, Tmean, and Trange produced in this study are
623 also available in netCDF format. The high-quality OI estimates merge reanalysis and station data, which can be useful
624 to applications that do not need ensemble forcings. The data sizes are 3.35 TB for the probabilistic part and 40.84 GB
625 for the deterministic part, respectively.

626 The ensemble mean of the 100 members for Tmean and Trange is similar to deterministic OI estimates. For
627 precipitation, the ensemble mean is slightly higher than deterministic OI estimates due to the back transformation. We
628 recommend that users select the deterministic dataset instead of the ensemble mean if their applications do not involve
629 uncertainty characterization.

630 A teaser dataset of probabilistic estimates is provided to facilitate easy preview of EMDNA without downloading the
631 entire dataset. The teaser dataset covers the region from -116.8° to -115.2°W, and 50.7° to 51.9°N, the time from 2014
632 to 2015, and the ensemble members from 1 to 25. The total data size is smaller than 30 MB. See Appendix E for a
633 brief introduction.

7. Summary and Conclusions

Ensemble meteorological datasets are of great value to hydrological and meteorological studies. Given the lack of a historical ensemble dataset for the entire North America, this study develops EMDNA by integrating multi-source information to overcome the limitation of sparse stations in high-latitude regions. EMDNA contains precipitation, Tmean, and Trange estimates at 0.1° spatial resolution and daily temporal resolution from 1979 to 2018 with 100 members. Multiple methodological choices are examined when determining critical steps in the production of EMDNA. The ultimate framework composes of four main steps: (1) generating station-based interpolation estimates from SCDNA using locally weighted linear/logistic regression, (2) regridding, correction, and merging of reanalysis products (ERA5, MERRA-2, and JRA-55), (3) merging station-reanalysis estimates using OI based on a novel method of OI weight calculation, and correcting precipitation under-catch using the PBCOR dataset, and (4) generating ensemble estimates by sampling from the estimated probability distributions with the perturbations provided by SCRF.

The performance of each step is comprehensively evaluated using multiple methods. The results show that the design of the framework is effective. In short, we find that (1) station-based interpolation estimates are less accurate in regions with sparse stations (e.g., high latitudes) and complex terrain; (2) BMA-merged reanalysis estimates show notable improvement against raw reanalysis estimates, particularly for precipitation and Trange and over high-latitude regions; (3) OI achieves more accurate estimates than interpolation and reanalysis estimates from (1) and (2), respectively, and the complementary effect between reanalysis and interpolation estimates contributes to the large improvement of OI estimates in sparsely gauged regions; and (4) ensemble precipitation estimates show good discrimination and reliability performance for all thresholds, and the BSS values for ensemble precipitation and CRPSS values for ensemble Tmean and Trange are high in most cases. BSS values of ensemble precipitation increase from 1979 to 2018 due to the increase in the number of stations.

Overall, EMDNA (version 1) will be useful for many applications in North America such as regional or continental hydrological modeling. Meanwhile, we recognize that the current framework is not perfect and have provided suggestions on the future directions for large-scale ensemble estimation of meteorological variables. Continuing efforts from the community are needed to promote the development of probabilistic estimation methods and datasets. Development of datasets at higher resolutions (e.g., 1 km and hourly) is also an important direction to enable more sophisticated hydrometeorological studies (e.g., Sampson et al., 2020).

Author contributions: GT and MC designed the framework of this study. GT collected data, performed the analyses and wrote the paper. MC, SP, AN and AW contributed to the design of the methodology and result evaluation. SP, DB and PW contributed to the evaluation of methodology and results. All authors contributed to data analysis, discussions about the methods and results, and paper improvement.

Competing interests: The authors declare that they have no conflict of interest.

667 **Acknowledgment:** The study is funded by the Global Water Futures (GWF) program in Canada. The authors
668 appreciate the extensive efforts from the developers of the ground and reanalysis datasets to make their products
669 available. The authors also thank Federated Research Data Repository (FRDR; https://www.frdr-dfdr.ca; Access Date:
670 September 29, 2020) for publishing our dataset as open access to users.

671

Appendix A. Regression coefficients

673 The coefficients for locally weight linear regression are estimated using weighted least squares. Given a station i with
674 m neighboring stations, let $\mathbf{A} = [1, A_1, \dots, A_n]$ be the $m \times n + 1$ attribute matrix, let $\mathbf{x} = (x_1, x_2, \dots, x_m)$ be the station
675 observations from neighboring stations, and let $\mathbf{w}_i = (w_{i,1}, w_{i,2}, \dots, w_{i,m})$ be the weight vector with distance-based
676 weights computed from Eq. (5). The regression coefficients $\boldsymbol{\beta} = (\beta_0, \beta_1, \dots, \beta_n)$ for Eq. (4) are estimated from the
677 weighted normal equation as

$$\boldsymbol{\beta} = (\mathbf{A}^\mathrm{T}\mathbf{W}\mathbf{A})^{-1}\mathbf{A}^\mathrm{T}\mathbf{W}\mathbf{x}, \qquad\qquad \text{A1}$$

678 where the $m \times m$ weight matrix $\mathbf{W} = \mathbf{I}_m\mathbf{w}_i$ is a diagonal matrix obtained by multiplying the $m \times m$ identity matrix
679 $\mathbf{I}_m$ with the weight vector $\mathbf{w}_i$.

680 The regression coefficients for logistic regression (Eq. 6) are estimated iteratively as:

$$\boldsymbol{\beta}^{new} = \boldsymbol{\beta}^{old} + (\mathbf{A}^\mathrm{T}\mathbf{W}\mathbf{V}\mathbf{A})^{-1}\mathbf{A}^\mathrm{T}\mathbf{W}(\mathbf{P}_0 - \boldsymbol{\pi}) \qquad\qquad \text{A2}$$

$$\boldsymbol{\pi} = \frac{1}{1 + \exp(-\mathbf{A}\boldsymbol{\beta}^{old})} \qquad\qquad \text{A3}$$

$$\mathbf{V} = \mathbf{I}_m\boldsymbol{\pi}(1 - \boldsymbol{\pi}) \qquad\qquad \text{A4}$$

681 where $\mathbf{P}_0$ is a vector of binary precipitation occurrence for neighboring stations, $\boldsymbol{\pi}$ is the vector of estimated PoP for
682 neighboring stations, and $\mathbf{V}$ is the diagonal variance matrix for PoP. The regression coefficients $\boldsymbol{\beta}^{old}$ are initialized as
683 a vector of ones.

684

Appendix B. Anomalous stations

686 To exclude climatologically anomalous stations, for temperature (Tmean or Trange), we calculate: (1) the absolute
687 difference of the climatological mean between the target station and the average value of its 10 neighboring stations

688   (referred to as Diff-1), and (2) the absolute difference of the climatological mean between station observation and

689   regression estimates (referred as Diff-2). A temperature station will be excluded if its Diff-1 is larger than the 95%

690   percentile and its Diff-2 larger than the 99% percentile of all stations simultaneously. The threshold of percentiles for

691   Diff-1 is lower to better identify some climatologically anomalous stations.

692   For precipitation, the ratio (Ratio-1 and Ratio-2) is obtained in the same way with the Diff-1 and Diff-2 of temperature.

693   A two-tailed check is used for precipitation compared with the one-tailed check for temperature. A precipitation station

694   will be excluded if its Ratio-1 is larger (or smaller) than the 99.9% (1%) percentile and its Ratio-2 larger (or smaller)

695   than the 99.9% (1%) percentile simultaneously. This check has more tolerance for heavy precipitation but tries to

696   exclude more extremely dry stations.

697   As a result, ~1.5% precipitation and temperature stations are rejected, after which algorithms described in Sect. 3.1.1

698   and 3.1.2 are re-run. Stations can be anomalous because they are badly operated or simply because they are unique in

699   terms of topography or climate. The usage of Diff-2 or Ratio-2 is helpful to avoid excluding unique stations, but for

700   cases where the regression is ineffective, the unique stations can still be wrongly excluded. Although the effect on

701   final estimates could be rather small, better strategies could be used in future studies.

702

Appendix C. Error of BMA-merged reanalysis estimates

704   The errors of BMA-merged estimates are first estimated for all stations and then interpolated to grids. Considering

705   station observations cannot be used to evaluate merged estimates once they are used in bias correction or BMA weight

706   estimation, a two-layer cross-validation strategy is designed. In the first layer, we treat i as the target station and find

707   its m ($j_1 = 1, 2, ..., m$; $i \notin j_1$) neighboring stations. In the second layer, we treat each j_1 as a target station, and (1)

708   find m ($j_2 = 1, 2, ..., m$; $i \notin j_2$) neighboring stations for each j_1, (2) calculate linear scaling correction factors for all

709   j_2, (3) estimate the correction factor for the target j_1 by interpolating factors at all j_2 stations using inverse distance

710   weighting, (4) correct estimates at j_1 using the correction factor, (5) calculate BMA weights of three reanalysis

711   products for all j_1 stations, (6) interpolate BMA weights from all j_1 stations to the target station i and merge the three

712   reanalysis products for i, and (7) calculate the difference between merged reanalysis estimates and station observations

713   for i. This two-layer design may seem convoluted but is necessary to ensure that the error estimation is realistic. j_1

714   and j_2 could be partly overlapped due to their close locations but should not cause a large effect on the error estimation

715   for i because data for i are only used in (7) in this design. The station-based errors are interpolated to all grids using

716   inverse distance weighting.

Appendix D. Metrics for probabilistic evaluation

718   BSS is calculated based on the Brier Score (BS):

$$BSS = 1 - \frac{BS}{BS_{clim}} \qquad\qquad D1$$

$$BS = \frac{1}{n}\sum_{i=1}^{n} (PoP_{ens} - PoP_{obs})^2 \qquad\qquad D2$$

719   where PoP_{ens} is the estimated probability of ensemble precipitation, PoP_{obs} is the observed binary precipitation
720   occurrence, n is the sample number, and BS_{clim} is the climatological BS by assigning the climatological probability
721   to all samples. When the two series match the value of BSS will be equal to one.

722   CRPSS is calculated based on the continuous ranked probability skill score (CRPS; Hersbach, 2000):

$$CRPSS = 1 - \frac{CRPS}{CRPS_{clim}} \qquad\qquad D3$$

$$CRPS = \int_{-\infty}^{\infty} (F(x) - H(x \geq x_o))^2 dx \qquad\qquad D4$$

723   where $F(x)$ is the CDF of the ensemble temperature estimate x, x_o is the observed temperature, $H(x \geq x_o)$ is the
724   Heaviside step function with the value being one if the condition $x \geq x_o$ is satisfied and zero if not satisfied, and
725     $CRPS_{clim}$ is the climatological CPRS. CRPS measures the distance between the CDF of probabilistic estimates and
726   observations. For a perfect match, the value of CRPSS would be one.

Appendix E. Teaser dataset

728   The teaser dataset is a subset of EMDNA probabilistic estimates for a small region (-116.8° to -115.2°W, 50.7° to
729   51.9°N) and a short period (2014 to 2015) with only 25 ensemble members. Users can easily download and preview
730   the teaser dataset (<30 MB) before downloading the entire EMDNA dataset (~3 TB or ~40 GB) as shown in Sect. 6.
731   The region covers the Bow River basin above Banff, Canada, which is located in the Canadian Rockies (Figure A1).
732   The spread of ensemble members in this region could be large due to the complex topography and limited stations.

733
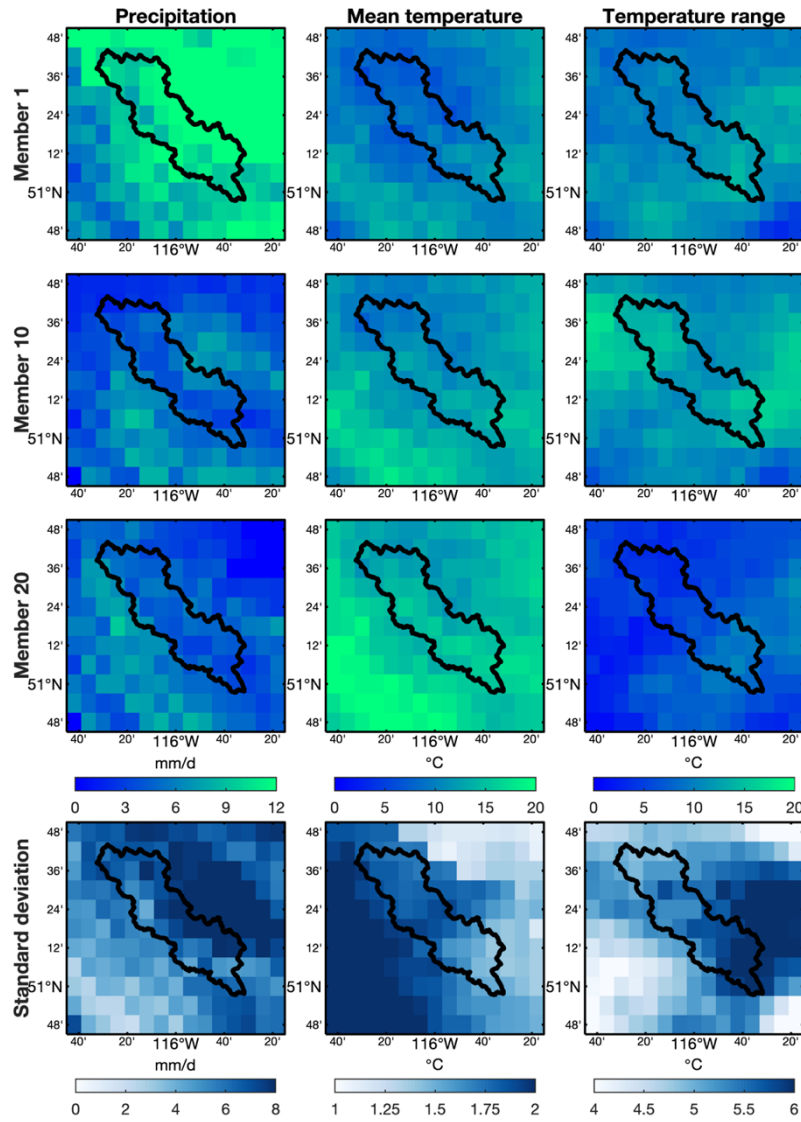
Figure A1. The distributions of daily precipitation (the first column), mean daily temperature (the second column), and daily temperature range (the third column) on 29 June 2015. The first to third rows represent ensemble members 1, 10, and 20, respectively. The fourth row represents the standard deviation of 25 members for this day. The black line outlines the Bow River basin above Banff, Canada.

738

References

Aalto, J., Pirinen, P., and Jylhä, K.: New gridded daily climatology of Finland: Permutation-based uncertainty estimates and temporal trends in climate, J. Geophys. Res. Atmospheres, 121, 3807–3823, https://doi.org/10.1002/2015JD024651, 2016.

743 Adler, R. F., Gu, G. J., Sapiano, M., Wang, J. J., and Huffman, G. J.: Global Precipitation: Means, Variations and
744 Trends During the Satellite Era (1979-2014), Surv. Geophys., 38, 679–699, https://doi.org/10.1007/s10712-017-9416-
745 4, 2017.

746 Arias-Hidalgo, M., Bhattacharya, B., Mynett, A. E., and van Griensven, A.: Experiences in using the TMPA-3B42R
747 satellite data to complement rain gauge measurements in the Ecuadorian coastal foothills, Hydrol. Earth Syst. Sci., 17,
748 2905–2915, https://doi.org/10.5194/hess-17-2905-2013, 2013.

749 Beck, H. E., Vergopolan, N., Pan, M., Levizzani, V., van Dijk, A. I. J. M., Weedon, G., Brocca, L., Pappenberger, F.,
750 Huffman, G. J., and Wood, E. F.: Global-scale evaluation of 23 precipitation datasets using gauge observations and
751 hydrological modeling, Hydrol. Earth Syst. Sci., 21, 6201–6217, https://doi.org/10.5194/hess-2017-508, 2017.

752 Beck, H. E., Wood, E. F., Pan, M., Fisher, C. K., Miralles, D. G., van Dijk, A. I. J. M., McVicar, T. R., and Adler, R.
753 F.: MSWEP V2 Global 3-Hourly 0.1° Precipitation: Methodology and Quantitative Assessment, Bull. Am. Meteorol.
754 Soc., 100, 473–500, https://doi.org/10.1175/BAMS-D-17-0138.1, 2019.

755 Beck, H. E., Wood, E. F., McVicar, T. R., Zambrano-Bigiarini, M., Alvarez-Garreton, C., Baez-Villanueva, O. M.,
756 Sheffield, J., and Karger, D. N.: Bias Correction of Global High-Resolution Precipitation Climatologies Using
757 Streamflow Observations from 9372 Catchments, J. Clim., 33, 1299–1315, https://doi.org/10.1175/JCLI-D-19-0332.1,
758 2020.

759 Brier, G. W.: Verification of forecasts expressed in terms of probability, Mon. Weather Rev., 78, 1–3,
760 https://doi.org/10.1175/1520-0493(1950)078<0001:VOFEIT>2.0.CO;2, 1950.

761 Bromwich, D. H., Wilson, A. B., Bai, L., Liu, Z., Barlage, M., Shih, C.-F., Maldonado, S., Hines, K. M., Wang, S.-
762 H., and Woollen, J.: The Arctic system reanalysis, version 2, Bull. Am. Meteorol. Soc., 99, 805–828, 2018.

763 Caillouet, L., Vidal, J.-P., Sauquet, E., Graff, B., and Soubeyroux, J.-M.: SCOPE Climate: a 142-year daily high-
764 resolution ensemble meteorological reconstruction dataset over France, Earth Syst. Sci. Data, 11, 241–260,
765 https://doi.org/10.5194/essd-11-241-2019, 2019.

766 Cannon, A. J., Sobie, S. R., and Murdock, T. Q.: Bias Correction of GCM Precipitation by Quantile Mapping: How
767 Well Do Methods Preserve Changes in Quantiles and Extremes?, J. Clim., 28, 6938–6959,
768 https://doi.org/10.1175/JCLI-D-14-00754.1, 2015.

769 Chen, Y., Yuan, W., Xia, J., Fisher, J. B., Dong, W., Zhang, X., Liang, S., Ye, A., Cai, W., and Feng, J.: Using
770 Bayesian model averaging to estimate terrestrial evapotranspiration in China, J. Hydrol., 528, 537–549,
771 https://doi.org/10.1016/j.jhydrol.2015.06.059, 2015.

772 Clark, M. P. and Hay, L. E.: Use of medium-range numerical weather prediction model output to produce forecasts of
773 streamflow, J. Hydrometeorol., 5, 15–32, 2004.

774 Clark, M. P. and Slater, A. G.: Probabilistic Quantitative Precipitation Estimation in Complex Terrain, J.
775 Hydrometeorol., 7, 3–22, https://doi.org/10.1175/JHM474.1, 2006.

776 Clark, M. P., Slater, A. G., Barrett, A. P., Hay, L. E., McCabe, G. J., Rajagopalan, B., and Leavesley, G. H.:
777 Assimilation of snow covered area information into hydrologic and land-surface models, Adv. Water Resour., 29,
778 1209–1221, https://doi.org/10.1016/j.advwatres.2005.10.001, 2006.

779 Cornes, R. C., Schrier, G. van der, Besselaar, E. J. M. van den, and Jones, P. D.: An ensemble version of the E-OBS
780 temperature and precipitation data sets, J. Geophys. Res. Atmospheres, 123, 9391–9409,
781 https://doi.org/10.1029/2017JD028200, 2018.

782 Daly, C., Halbleib, M., Smith, J. I., Gibson, W. P., Doggett, M. K., Taylor, G. H., Curtis, J., and Pasteris, P. P.:
783 Physiographically sensitive mapping of climatological temperature and precipitation across the conterminous United
784 States, Int. J. Climatol., 28, 2031–2064, https://doi.org/10.1002/joc.1688, 2008.

785 Di Luzio, M., Johnson, G. L., Daly, C., Eischeid, J. K., and Arnold, J. G.: Constructing Retrospective Gridded Daily
786 Precipitation and Temperature Datasets for the Conterminous United States, J. Appl. Meteorol. Climatol., 47, 475–
787 497, https://doi.org/10.1175/2007JAMC1356.1, 2008.

788 Dinku, T., Anagnostou, E. N., and Borga, M.: Improving radar-based estimation of rainfall over complex terrain, J.
789 Appl. Meteorol., 41, 1163–1178, 2002.

790 Donat, M. G., Sillmann, J., Wild, S., Alexander, L. V., Lippmann, T., and Zwiers, F. W.: Consistency of Temperature
791 and Precipitation Extremes across Various Global Gridded In Situ and Reanalysis Datasets, J. Clim., 27, 5019–5035,
792 https://doi.org/10.1175/JCLI-D-13-00405.1, 2014.

793 Duan, Q. and Phillips, T. J.: Bayesian estimation of local signal and noise in multimodel simulations of climate change,
794 J. Geophys. Res. Atmospheres, 115, https://doi.org/10.1029/2009JD013654, 2010.

795 Duan, S.-B. and Li, Z.-L.: Spatial Downscaling of MODIS Land Surface Temperatures Using Geographically
796 Weighted Regression: Case Study in Northern China, IEEE Trans. Geosci. Remote Sens., 54, 6458–6469,
797 https://doi.org/10.1109/TGRS.2016.2585198, 2016.

798 Eischeid, J. K., Pasteris, P. A., Diaz, H. F., Plantico, M. S., and Lott, N. J.: Creating a Serially Complete, National
799 Daily Time Series of Temperature and Precipitation for the Western United States, J. Appl. Meteorol., 39, 1580–1591,
800 https://doi.org/10.1175/1520-0450(2000)039<1580:CASCND>2.0.CO;2, 2000.

801 Fick, S. E. and Hijmans, R. J.: WorldClim 2: new 1-km spatial resolution climate surfaces for global land areas, Int.
802 J. Climatol., 37, 4302–4315, 2017.

803 Folland, C. K.: Numerical models of the raingauge exposure problem, field experiments and an improved collector
804 design, Q. J. R. Meteorol. Soc., 114, 1485–1516, https://doi.org/10.1002/qj.49711448407, 1988.

805 Fortin, V., Roy, G., Donaldson, N., and Mahidjiba, A.: Assimilation of radar quantitative precipitation estimations in
806 the Canadian Precipitation Analysis (CaPA), J. Hydrol., 531, 296–307, https://doi.org/10.1016/j.jhydrol.2015.08.003,
807 2015.

808 Fortin, V., Roy, G., Stadnyk, T., Koenig, K., Gasset, N., and Mahidjiba, A.: Ten Years of Science Based on the
809 Canadian Precipitation Analysis: A CaPA System Overview and Literature Review, Atmosphere-Ocean, 56, 178–196,
810 https://doi.org/10.1080/07055900.2018.1474728, 2018.

811 Frei, C. and Isotta, F. A.: Ensemble Spatial Precipitation Analysis From Rain Gauge Data: Methodology and
812 Application in the European Alps, J. Geophys. Res. Atmospheres, 124, 5757–5778,
813 https://doi.org/10.1029/2018JD030004, 2019.

814 Fuchs, T., Rapp, J., Rubel, F., and Rudolf, B.: Correction of synoptic precipitation observations due to systematic
815 measuring errors with special regard to precipitation phases, Phys. Chem. Earth Part B Hydrol. Oceans Atmosphere,
816 26, 689–693, 2001.

817 Funk, C., Peterson, P., Landsfeld, M., Pedreros, D., Verdin, J., Shukla, S., Husak, G., Rowland, J., Harrison, L., Hoell,
818 A., and Michaelsen, J.: The climate hazards infrared precipitation with stations--a new environmental record for
819 monitoring extremes, Sci. Data, 2, 150066, https://doi.org/10.1038/sdata.2015.66, 2015.

820 Gelaro, R., McCarty, W., Suárez, M. J., Todling, R., Molod, A., Takacs, L., Randles, C. A., Darmenov, A., Bosilovich,
821 M. G., Reichle, R., Wargan, K., Coy, L., Cullather, R., Draper, C., Akella, S., Buchard, V., Conaty, A., da Silva, A.
822 M., Gu, W., Kim, G.-K., Koster, R., Lucchesi, R., Merkova, D., Nielsen, J. E., Partyka, G., Pawson, S., Putman, W.,

Rienecker, M., Schubert, S. D., Sienkiewicz, M., and Zhao, B.: The Modern-Era Retrospective Analysis for Research and Applications, Version 2 (MERRA-2), J. Clim., 30, 5419–5454, https://doi.org/10.1175/jcli-d-16-0758.1, 2017.

Goodison, B. E., Louie, P. Y., and Yang, D.: WMO solid precipitation measurement intercomparison, 1998.

Habib, E., Haile, A. T., Sazib, N., Zhang, Y., and Rientjes, T.: Effect of Bias Correction of Satellite-Rainfall Estimates on Runoff Simulations at the Source of the Upper Blue Nile, Remote Sens., 6, 6688–6708, https://doi.org/10.3390/rs6076688, 2014.

Hamilton, A. S. and Moore, R. D.: Quantifying Uncertainty in Streamflow Records, Can. Water Resour. J. Rev. Can. Ressour. Hydr., 37, 3–21, https://doi.org/10.4296/cwrj3701865, 2012.

Harris, I., Osborn, T. J., Jones, P., and Lister, D.: Version 4 of the CRU TS monthly high-resolution gridded multivariate climate dataset, Sci. Data, 7, 109, https://doi.org/10.1038/s41597-020-0453-3, 2020.

Haylock, M. R., Hofstra, N., Klein Tank, A. M. G., Klok, E. J., Jones, P. D., and New, M.: A European daily high-resolution gridded data set of surface temperature and precipitation for 1950–2006, J. Geophys. Res. Atmospheres, 113, https://doi.org/10.1029/2008JD010201, 2008.

Hellinger, E.: Neue begründung der theorie quadratischer formen von unendlichvielen veränderlichen., J. Für Reine Angew. Math. Crelles J., 1909, 210–271, 1909.

Hempel, S., Frieler, K., Warszawski, L., Schewe, J., and Piontek, F.: A trend-preserving bias correction – the ISI-MIP approach, Earth Syst. Dyn., 4, 219–236, https://doi.org/10.5194/esd-4-219-2013, 2013.

Henn, B., Newman, A. J., Livneh, B., Daly, C., and Lundquist, J. D.: An assessment of differences in gridded precipitation datasets in complex terrain, J. Hydrol., 556, 1205–1219, https://doi.org/10.1016/j.jhydrol.2017.03.008, 2018.

Herrnegger, M., Senoner, T., and Nachtnebel, H.-P.: Adjustment of spatio-temporal precipitation patterns in a high Alpine environment, J. Hydrol., 556, 913–921, https://doi.org/10.1016/j.jhydrol.2016.04.068, 2018.

Hersbach, H.: Decomposition of the continuous ranked probability score for ensemble prediction systems, Weather Forecast., 15, 559–570, 2000.

Hersbach, H., Bell, B., Berrisford, P., Hirahara, S., Horányi, A., Muñoz-Sabater, J., Nicolas, J., Peubey, C., Radu, R., Schepers, D., Simmons, A., Soci, C., Abdalla, S., Abellan, X., Balsamo, G., Bechtold, P., Biavati, G., Bidlot, J., Bonavita, M., Chiara, G. D., Dahlgren, P., Dee, D., Diamantakis, M., Dragani, R., Flemming, J., Forbes, R., Fuentes, M., Geer, A., Haimberger, L., Healy, S., Hogan, R. J., Hólm, E., Janisková, M., Keeley, S., Laloyaux, P., Lopez, P., Lupu, C., Radnoti, G., Rosnay, P. de, Rozum, I., Vamborg, F., Villaume, S., and Thépaut, J.-N.: The ERA5 global reanalysis, Q. J. R. Meteorol. Soc., 146, 1999–2049, https://doi.org/10.1002/qj.3803, 2020.

Hoeting, J. A., Madigan, D., Raftery, A. E., and Volinsky, C. T.: Bayesian Model Averaging: A Tutorial, Stat. Sci., 14, 382–401, 1999.

Hong, Y., Hsu, K., Moradkhani, H., and Sorooshian, S.: Uncertainty quantification of satellite precipitation estimation and Monte Carlo assessment of the error propagation into hydrologic response, Water Resour. Res., 42, https://doi.org/10.1029/2005wr004398, 2006.

Hu, Q., Li, Z., Wang, L., Huang, Y., Wang, Y., and Li, L.: Rainfall Spatial Estimations: A Review from Spatial Interpolation to Multi-Source Data Merging, Water, 11, 579, https://doi.org/10.3390/w11030579, 2019.

Huffman, G. J., Bolvin, D. T., Nelkin, E. J., Wolff, D. B., Adler, R. F., Gu, G., Hong, Y., Bowman, K. P., and Stocker, E. F.: The TRMM Multisatellite Precipitation Analysis (TMPA): Quasi-Global, Multiyear, Combined-Sensor Precipitation Estimates at Fine Scales, J. Hydrometeorol., 8, 38–55, https://doi.org/10.1175/jhm560.1, 2007.

863   Karger, D. N., Conrad, O., Bohner, J., Kawohl, T., Kreft, H., Soria-Auza, R. W., Zimmermann, N. E., Linder, H. P.,
864   and Kessler, M.: Climatologies at high resolution for the earth's land surface areas, Sci. Data, 4, 170122,
865   https://doi.org/10.1038/sdata.2017.122, 2017.

866   Kemp, W. P., Burnell, D. G., Everson, D. O., and Thomson, A. J.: Estimating Missing Daily Maximum and Minimum
867   Temperatures, J. Clim. Appl. Meteorol., 22, 1587–1593, https://doi.org/10.1175/1520-
868   0450(1983)022<1587:EMDMAM>2.0.CO;2, 1983.

869   Khedhaouiria, D., Bélair, S., Fortin, V., Roy, G., and Lespinas, F.: High Resolution (2.5km) Ensemble Precipitation
870   Analysis across Canada, J. Hydrometeorol., https://doi.org/10.1175/JHM-D-19-0282.1, 2020.

871   Kiang, J. E., Gazoorian, C., McMillan, H., Coxon, G., Coz, J. L., Westerberg, I. K., Belleville, A., Sevrez, D., Sikorska,
872   A. E., Petersen-Øverleir, A., Reitan, T., Freer, J., Renard, B., Mansanarez, V., and Mason, R.: A Comparison of
873   Methods for Streamflow Uncertainty Estimation, Water Resour. Res., 54, 7149–7176,
874   https://doi.org/10.1029/2018WR022708, 2018.

875   Kirstetter, P.-E., Gourley, J. J., Hong, Y., Zhang, J., Moazamigoodarzi, S., Langston, C., and Arthur, A.: Probabilistic
876   precipitation rate estimates with ground-based radar networks, Water Resour. Res., 51, 1422–1442,
877   https://doi.org/10.1002/2014WR015672, 2015.

878   Kobayashi, S., Ota, Y., Harada, Y., Ebita, A., Moriya, M., Onoda, H., Onogi, K., Kamahori, H., Kobayashi, C., Endo,
879   H., Miyaoka, K., and Takahashi, K.: The JRA-55 Reanalysis: General Specifications and Basic Characteristics, J.
880   Meteorol. Soc. Jpn. Ser II, 93, 5–48, https://doi.org/10.2151/jmsj.2015-001, 2015.

881   Kochendorfer, J., Nitu, R., Wolff, M., Mekis, E., Rasmussen, R., Baker, B., Earle, M. E., Reverdin, A., Wong, K.,
882   Smith, C. D., Yang, D., Roulet, Y.-A., Meyers, T., Buisan, S., Isaksen, K., Brækkan, R., Landolt, S., and Jachcik, A.:
883   Testing and development of transfer functions for weighing precipitation gauges in WMO-SPICE, Hydrol. Earth Syst.
884   Sci., 22, 1437–1452, https://doi.org/10.5194/hess-22-1437-2018, 2018.

885   Lader, R., Bhatt, U. S., Walsh, J. E., Rupp, T. S., and Bieniek, P. A.: Two-Meter Temperature and Precipitation from
886   Atmospheric Reanalysis Evaluated for Alaska, J. Appl. Meteorol. Climatol., 55, 901–922,
887   https://doi.org/10.1175/JAMC-D-15-0162.1, 2016.

888   Livneh, B., Rosenberg, E. A., Lin, C., Nijssen, B., Mishra, V., Andreadis, K. M., Maurer, E. P., and Lettenmaier, D.
889   P.: A Long-Term Hydrologically Based Dataset of Land Surface Fluxes and States for the Conterminous United States:
890   Update and Extensions, J. Clim., 26, 9384–9392, https://doi.org/10.1175/JCLI-D-12-00508.1, 2013.

891   Longman, R. J., Newman, A. J., Giambelluca, T. W., and Lucas, M.: Characterizing the Uncertainty and Assessing
892   the Value of Gap-Filled Daily Rainfall Data in Hawaii, J. Appl. Meteorol. Climatol., 59, 1261–1276,
893   https://doi.org/10.1175/JAMC-D-20-0007.1, 2020.

894   Lu, X., Tang, G., Wang, X., Liu, Y., Wei, M., and Zhang, Y.: The Development of a Two-Step Merging and
895   Downscaling Method for Satellite Precipitation Products, Remote Sens., 12, 398, 2020.

896   Ma, Y., Yang, Y., Han, Z., Tang, G., Maguire, L., Chu, Z., and Hong, Y.: Comprehensive evaluation of Ensemble
897   Multi-Satellite Precipitation Dataset using the Dynamic Bayesian Model Averaging scheme over the Tibetan plateau,
898   J. Hydrol., 556, 634–644, https://doi.org/10.1016/j.jhydrol.2017.11.050, 2018a.

899   Ma, Y., Hong, Y., Chen, Y., Yang, Y., Tang, G., Yao, Y., Long, D., Li, C., Han, Z., and Liu, R.: Performance of
900   Optimally Merged Multisatellite Precipitation Products Using the Dynamic Bayesian Model Averaging Scheme Over
901   the Tibetan Plateau, J. Geophys. Res. Atmospheres, 123, 814–834, https://doi.org/10.1002/2017jd026648, 2018b.

902   Ma, Z., Xu, J., Zhu, S., Yang, J., Tang, G., Yang, Y., Shi, Z., and Hong, Y.: AIMERG: a new Asian precipitation
903   dataset (0.1°/half-hourly, 2000–2015) by calibrating the GPM-era IMERG at a daily scale using APHRODITE, Earth
904   Syst. Sci. Data, 12, 1525–1544, https://doi.org/10.5194/essd-12-1525-2020, 2020.

905 Mahfouf, J.-F., Brasnett, B., and Gagnon, S.: A Canadian precipitation analysis (CaPA) project: Description and
906 preliminary results, Atmosphere-Ocean, 45, 1–17, https://doi.org/10.3137/ao.v450101, 2007.

907 Maurer, E. P., Wood, A. W., Adam, J. C., Lettenmaier, D. P., and Nijssen, B.: A Long-Term Hydrologically Based
908 Dataset of Land Surface Fluxes and States for the Conterminous United States, J. Clim., 15, 15, 2002.

909 Mears, C. A., Wentz, F. J., Thorne, P., and Bernie, D.: Assessing uncertainty in estimates of atmospheric temperature
910 changes from MSU and AMSU using a Monte-Carlo estimation technique, J. Geophys. Res. Atmospheres, 116,
911 https://doi.org/10.1029/2010JD014954, 2011.

912 Mendoza, P. A., Wood, A. W., Clark, E., Rothwell, E., Clark, M. P., Nijssen, B., Brekke, L. D., and Arnold, J. R.: An
913 intercomparison of approaches for improving operational seasonal streamflow forecasts, Hydrol. Earth Syst. Sci., 21,
914 3915–3935, 2017.

915 Mooney, P. A., Mulligan, F. J., and Fealy, R.: Comparison of ERA-40, ERA-Interim and NCEP/NCAR reanalysis
916 data with observed surface air temperatures over Ireland, Int. J. Climatol., 31, 545–557,
917 https://doi.org/10.1002/joc.2098, 2011.

918 Morice, C. P., Kennedy, J. J., Rayner, N. A., and Jones, P. D.: Quantifying uncertainties in global and regional
919 temperature change using an ensemble of observational estimates: The HadCRUT4 data set, J. Geophys. Res.
920 Atmospheres, 117, https://doi.org/10.1029/2011JD017187, 2012.

921 Muñoz-Sabater, J., Dutra, E., Agustí-Panareda, A., Albergel, C., Arduini, G., Balsamo, G., Boussetta, S., Choulga,
922 M., Harrigan, S., and Hersbach, H.: ERA5-Land: A state-of-the-art global reanalysis dataset for land applications,
923 Earth Syst. Sci. Data Discuss., 1–50, 2021.

924 Nešpor, V. and Sevruk, B.: Estimation of Wind-Induced Error of Rainfall Gauge Measurements Using a Numerical
925 Simulation, J. Atmospheric Ocean. Technol., 16, 450–464, https://doi.org/10.1175/1520-
926 0426(1999)016<0450:EOWIEO>2.0.CO;2, 1999.

927 Newman, A. J. and Clark, M. P.: TIER version 1.0: an open-source Topographically InformEd Regression (TIER)
928 model to estimate spatial meteorological fields, Geosci. Model Dev., 13, 1827–1843, https://doi.org/10.5194/gmd-13-
929 1827-2020, 2020.

930 Newman, A. J., Clark, M. P., Craig, J., Nijssen, B., Wood, A., Gutmann, E., Mizukami, N., Brekke, L., and Arnold,
931 J. R.: Gridded Ensemble Precipitation and Temperature Estimates for the Contiguous United States, J. Hydrometeorol.,
932 16, 2481–2500, https://doi.org/10.1175/JHM-D-15-0026.1, 2015.

933 Newman, A. J., Clark, M. P., Longman, R. J., and Giambelluca, T. W.: Methodological Intercomparisons of Station-
934 Based Gridded Meteorological Products: Utility, Limitations, and Paths Forward, J. Hydrometeorol., 20, 531–547,
935 https://doi.org/10.1175/JHM-D-18-0114.1, 2019a.

936 Newman, A. J., Clark, M. P., Longman, R. J., Gilleland, E., Giambelluca, T. W., and Arnold, J. R.: Use of Daily
937 Station Observations to Produce High-Resolution Gridded Probabilistic Precipitation and Temperature Time Series
938 for the Hawaiian Islands, J. Hydrometeorol., 20, 509–529, https://doi.org/10.1175/JHM-D-18-0113.1, 2019b.

939 Newman, A. J., Clark, M. P., Wood, A. W., and Arnold, J. R.: Probabilistic Spatial Meteorological Estimates for
940 Alaska and the Yukon, J. Geophys. Res. Atmospheres, 2020.

941 Papalexiou, S. M.: Unified theory for stochastic modelling of hydroclimatic processes: Preserving marginal
942 distributions, correlation structures, and intermittency, Adv. Water Resour., 115, 234–252, 2018.

943 Papalexiou, S. M. and Koutsoyiannis, D.: Battle of extreme value distributions: A global survey on extreme daily
944 rainfall, Water Resour. Res., 49, 187–201, https://doi.org/10.1029/2012WR012557, 2013.

945   Papalexiou, S. M. and Serinaldi, F.: Random Fields Simplified: Preserving Marginal Distributions, Correlations, and
946   Intermittency, With Applications From Rainfall to Humidity, Water Resour. Res., 56, e2019WR026331,
947   https://doi.org/10.1029/2019WR026331, 2020.

948   Parker, W. S.: Reanalyses and Observations: What's the Difference?, Bull. Am. Meteorol. Soc., 97, 1565–1572,
949   https://doi.org/10.1175/BAMS-D-14-00226.1, 2016.

950   Raftery, A. E., Gneiting, T., Balabdaoui, F., and Polakowski, M.: Using Bayesian Model Averaging to Calibrate
951   Forecast Ensembles, Mon. Weather Rev., 133, 1155–1174, https://doi.org/10.1175/MWR2906.1, 2005.

952   Rodell, M., Beaudoing, H. K., L'Ecuyer, T. S., Olson, W. S., Famiglietti, J. S., Houser, P. R., Adler, R., Bosilovich,
953   M. G., Clayson, C. A., Chambers, D., Clark, E., Fetzer, E. J., Gao, X., Gu, G., Hilburn, K., Huffman, G. J., Lettenmaier,
954   D. P., Liu, W. T., Robertson, F. R., Schlosser, C. A., Sheffield, J., and Wood, E. F.: The Observed State of the Water
955   Cycle in the Early Twenty-First Century, J. Clim., 28, 8289–8318, https://doi.org/10.1175/JCLI-D-14-00555.1, 2015.

956   Sampson, A. A., Wright, D. B., Stewart, R. D., and LoBue, A. C.: The role of rainfall temporal and spatial averaging
957   in seasonal simulations of the terrestrial water balance, Hydrol. Process., 34, 2531–2542,
958   https://doi.org/10.1002/hyp.13745, 2020.

959   Scaff, L., Yang, D., Li, Y., and Mekis, E.: Inconsistency in precipitation measurements across the Alaska–Yukon
960   border, The Cryosphere, 9, 2417–2428, https://doi.org/10.5194/tc-9-2417-2015, 2015.

961   Schepen, A. and Wang, Q. J.: Model averaging methods to merge operational statistical and dynamic seasonal
962   streamflow forecasts in Australia, Water Resour. Res., 51, 1797–1812, https://doi.org/10.1002/2014WR016163, 2015.

963   Sevruk, B.: International comparison of national precipitation gauges with a reference pit gauge., WMO Instrum. Obs.
964   Methods Rep. No 17, 111, 1984.

965   Shen, Y., Zhao, P., Pan, Y., and Yu, J. J.: A high spatiotemporal gauge-satellite merged precipitation analysis over
966   China, J. Geophys. Res.-Atmospheres, 119, 3063–3075, https://doi.org/10.1002/2013jd020686, 2014a.

967   Shen, Y., Zhao, P., Pan, Y., and Yu, J.: A high spatiotemporal gauge-satellite merged precipitation analysis over China,
968   J. Geophys. Res. Atmospheres, 119, 3063–3075, https://doi.org/10.1002/2013JD020686, 2014b.

969   Shen, Y., Hong, Z., Pan, Y., Yu, J., and Maguire, L.: China's 1 km Merged Gauge, Radar and Satellite Experimental
970   Precipitation Dataset, Remote Sens., 10, 264, https://doi.org/10.3390/rs10020264, 2018.

971   Sinclair, S. and Pegram, G.: Combining radar and rain gauge rainfall estimates using conditional merging,
972   Atmospheric Sci. Lett., 6, 19–22, https://doi.org/10.1002/asl.85, 2005.

973   Slater, A. G. and Clark, M. P.: Snow Data Assimilation via an Ensemble Kalman Filter, J. Hydrometeorol., 7, 478–
974   493, https://doi.org/10.1175/JHM505.1, 2006.

975   Sun, Q., Miao, C., Duan, Q., Ashouri, H., Sorooshian, S., and Hsu, K.-L.: A Review of Global Precipitation Data Sets:
976   Data Sources, Estimation, and Intercomparisons, Rev. Geophys., https://doi.org/10.1002/2017rg000574, 2018.

977   Tang, G., Zeng, Z., Long, D., Guo, X., Yong, B., Zhang, W., and Hong, Y.: Statistical and Hydrological Comparisons
978   between TRMM and GPM Level-3 Products over a Midlatitude Basin: Is Day-1 IMERG a Good Successor for TMPA
979   3B42V7?, J. Hydrometeorol., 17, 121–137, https://doi.org/10.1175/jhm-d-15-0059.1, 2016.

980   Tang, G., Behrangi, A., Long, D., Li, C., and Hong, Y.: Accounting for spatiotemporal errors of gauges: A critical
981   step to evaluate gridded precipitation products, J. Hydrol., 559, 294–306,
982   https://doi.org/10.1016/j.jhydrol.2018.02.057, 2018a.

983 Tang, G., Behrangi, A., Ma, Z., Long, D., and Hong, Y.: Downscaling of ERA-Interim Temperature in the Contiguous
984 United States and Its Implications for Rain–Snow Partitioning, J. Hydrometeorol., 19, 1215–1233,
985 https://doi.org/10.1175/jhm-d-18-0041.1, 2018b.

986 Tang, G., Clark, M. P., Papalexiou, S. M., Newman, A. J., Wood, A. W., Brunet, D., and Whitfield, P. H.: EMDNA:
987 Ensemble Meteorological Dataset for North America [Dataset], FRDR, https://doi.org/10.20383/101.0275, 2020a.

988 Tang, G., Clark, M. P., Papalexiou, S. M., Ma, Z., and Hong, Y.: Have satellite precipitation products improved over
989 last two decades? A comprehensive comparison of GPM IMERG with nine satellite and reanalysis datasets, Remote
990 Sens. Environ., 240, 111697, https://doi.org/10.1016/j.rse.2020.111697, 2020b.

991 Tang, G., Clark, M. P., Newman, A. J., Wood, A. W., Papalexiou, S. M., Vionnet, V., and Whitfield, P. H.: SCDNA:
992 a serially complete precipitation and temperature dataset for North America from 1979 to 2018, Earth Syst. Sci. Data,
993 12, 2381–2409, https://doi.org/10.5194/essd-12-2381-2020, 2020c.

994 Tang, G., Clark, M. P., and Papalexiou, S. M.: The use of serially complete station data to improve the temporal
995 continuity of gridded precipitation and temperature estimates, J. Hydrometeorol., 2021.

996 Teutschbein, C. and Seibert, J.: Bias correction of regional climate model simulations for hydrological climate-change
997 impact studies: Review and evaluation of different methods, J. Hydrol., 456–457, 12–29,
998 https://doi.org/10.1016/j.jhydrol.2012.05.052, 2012.

999 Trenberth, K. E., Dai, A., Rasmussen, R. M., and Parsons, D. B.: The Changing Character of Precipitation, Bull. Am.
1000 Meteorol. Soc., 84, 1205–1218, https://doi.org/10.1175/BAMS-84-9-1205, 2003.

1001 Vila, D. A., de Goncalves, L. G. G., Toll, D. L., and Rozante, J. R.: Statistical Evaluation of Combined Daily Gauge
1002 Observations and Rainfall Satellite Estimates over Continental South America, J. Hydrometeorol., 10, 533–543,
1003 https://doi.org/10.1175/2008JHM1048.1, 2009.

1004 Weedon, G. P., Balsamo, G., Bellouin, N., Gomes, S., Best, M. J., and Viterbo, P.: The WFDEI meteorological forcing
1005 data set: WATCH Forcing Data methodology applied to ERA-Interim reanalysis data, Water Resour. Res., 50, 7505–
1006 7514, https://doi.org/10.1002/2014wr015638, 2014.

1007 Willkofer, F., Schmid, F.-J., Komischke, H., Korck, J., Braun, M., and Ludwig, R.: The impact of bias correcting
1008 regional climate model results on hydrological indicators for Bavarian catchments, J. Hydrol. Reg. Stud., 19, 25–41,
1009 https://doi.org/10.1016/j.ejrh.2018.06.010, 2018.

1010 Wood, A. W., Leung, L. R., Sridhar, V., and Lettenmaier, D. P.: Hydrologic Implications of Dynamical and Statistical
1011 Approaches to Downscaling Climate Model Outputs, Clim. Change, 62, 189–216,
1012 https://doi.org/10.1023/B:CLIM.0000013685.99609.9e, 2004.

1013 Wu, H., Adler, R. F., Tian, Y., Huffman, G. J., Li, H., and Wang, J.: Real-time global flood estimation using satellite-
1014 based precipitation and a coupled land surface and routing model, Water Resour. Res., 50, 2693–2717,
1015 https://doi.org/10.1002/2013wr014710, 2014.

1016 Xie, P. and Xiong, A.-Y.: A conceptual model for constructing high-resolution gauge-satellite merged precipitation
1017 analyses, J. Geophys. Res. Atmospheres, 116, https://doi.org/10.1029/2011JD016118, 2011.

1018 Xu, S., Wu, C., Wang, L., Gonsamo, A., Shen, Y., and Niu, Z.: A new satellite-based monthly precipitation
1019 downscaling algorithm with non-stationary relationship between precipitation and land surface characteristics, Remote
1020 Sens. Environ., 162, 119–140, https://doi.org/10.1016/j.rse.2015.02.024, 2015.

1021 Yamazaki, D., Ikeshima, D., Tawatari, R., Yamaguchi, T., O'Loughlin, F., Neal, J. C., Sampson, C. C., Kanae, S., and
1022 Bates, P. D.: A high-accuracy map of global terrain elevations, Geophys. Res. Lett., 44, 5844–5853,
1023 https://doi.org/10.1002/2017GL072874, 2017.

1024 Yang, D., Goodison, B. E., Ishida, S., and Benson, C. S.: Adjustment of daily precipitation data at 10 climate stations
1025 in Alaska: Application of World Meteorological Organization intercomparison results, Water Resour. Res., 34, 241–
1026 256, https://doi.org/10.1029/97WR02681, 1998.

1027 Yang, D., Kane, D., Zhang, Z., Legates, D., and Goodison, B.: Bias corrections of long-term (1973-2004) daily
1028 precipitation data over the northern regions, Geophys. Res. Lett., 32, n/a-n/a, https://doi.org/10.1029/2005gl024057,
1029 2005.

1030 Yin, J., Gentine, P., Zhou, S., Sullivan, S. C., Wang, R., Zhang, Y., and Guo, S.: Large increase in global storm runoff
1031 extremes driven by climate and anthropogenic changes, Nat. Commun., 9, 4389, https://doi.org/10.1038/s41467-018-
1032 06765-2, 2018.

1033 Zhang, Y., Ren, Y., Ren, G., and Wang, G.: Bias Correction of Gauge Data and its Effect on Precipitation Climatology
1034 over Mainland China, J. Appl. Meteorol. Climatol., 58, 2177–2196, https://doi.org/10.1175/JAMC-D-19-0049.1, 2019.

1035